Monte Carlo simulation of charged-particle production in Heavy-Ion Collisions with EPOS4

Bachelor Thesis

Submitted by:
Alexander Marco Tiekötter

University of Münster
Institute of Nuclear Physics
AG Andronic / Klein-Bösing

First Referee: Prof. Dr. Anton Andronic
Second Referee: apl. Prof. Dr. Christian Klein-Bösing

Münster, September 2023

Contents

1 Introduction

Since over a century, humans are colliding particles in different forms in large machinery. This has extended the boundaries of humanities knowledge and resulted in not only new technologies but also fascinating new questions. Today, collision experiments are, for example, performed at the Large Hadron Collider (LHC) in Switzerland and France at the European Center for Nuclear Research (CERN). Colliding high-energy protons and nuclei, which move at a velocity close to the speed of light, produces many secondary particles. Furthermore, a new state of matter, commonly referred to as Quark-Gluon Plasma (QGP), can form if the collision partners are heavy enough and the density or temperature exceeds a critical value. The production of such particles and a QGP can be quantified by e.g., the transverse momentum p_{T}, the multiplicity N_{ch}, and pseudorapidity η. With the measurement of these quantities, one can extract plenty of information about what happened during the interaction. To do so, particle detectors are built around the collision point. However, these devices are not capable of differentiating between the physical effects that scientists wants to investigate and secondary processes happening in the detector as well as underground effects, collectively called detector effects. To assist the analysis of the data produced by such detectors, Monte Carlo simulations (MC) are used to generate collision events that are not influenced by detector effects. Data produced by simulations can also be used to test theoretical models.

This thesis tests the production of charged particles in the EPOS model implemented in the EPOS4 MC event generator. This is done by comparing the simulation results produced with EPOS4 to real datasets from the ALICE (A Large Ion Collider Experiment) experiment at the LHC. The production of charged particles in collisions of protons with protons (pp), protons with lead nuclei (p-Pb), and lead with lead (Pb-Pb) is simulated, and the differences between the simulated and experimentally determined distributions are described. The structure of this thesis is as follows: Chapter 2 describes the theoretical background necessary to understand the processes and theories used in the analysis of heavy-ion collisions. This is followed by a description of the experimental setup at the LHC in chapter 4. The EPOS model and the simulation software are described shortly in chapter 5. The analysis of the produced data is then done in chapter 6. The analysis is concluded, and an outlook is provided in chapter 7.

2 Theoretical Background

In this chapter, the theoretical background for this thesis will be discussed. First, the standard model of particle physics with its contents is introduced, together with the theory of Quantum Chromodynamics. Afterwards, the quark-gluon plasma is introduced followed by a description of the kinematic variables in heavy-ion collisions. The Glauber model is then introduced to describe the geometry of the collision of heavy ions. The last section introduces some experimental observations in heavy-ion collisions.

2.1 The Standard Model and Quantum Chromodynamics

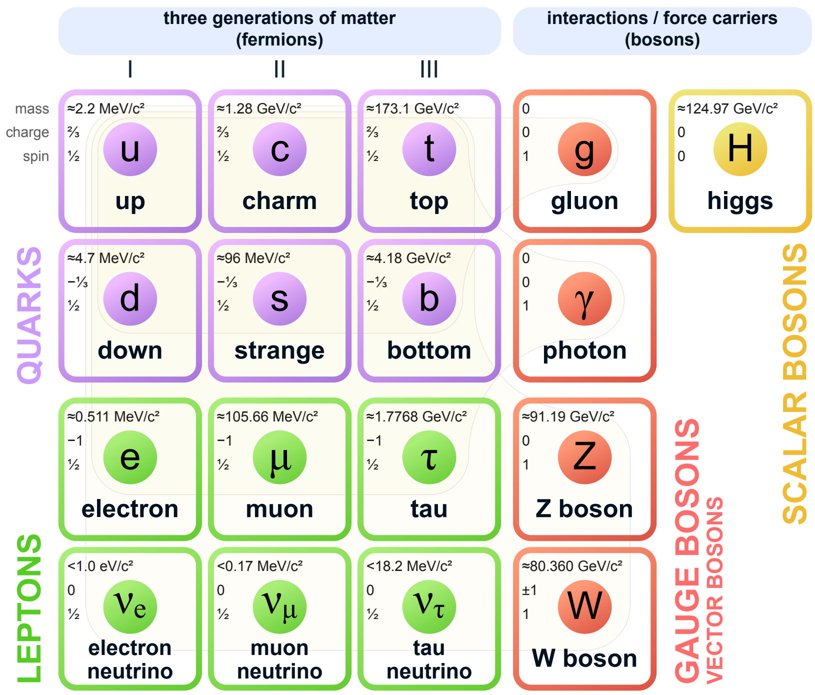

Figure 2.1: The Standard Model of particle physics [Mis23].

The Standard Model builds the theoretical foundation of particle physics [Tho13]. In its current form, it predicts 17 elementary particles: six quarks, six leptons, four vector bosons, and one scalar boson. The quarks and leptons are divided into three generations and build up massive particles like hadrons and mesons. The vector bosons are the carrier particles of three of the four fundamental forces and the scalar boson, the Higgs-Boson, is part of the Higgs-mechanism which is responsible for the mass of the four vector bosons. The only fundamental force that cannot be explained by the standard model is gravity. An overview of the particles in the standard model with their most important properties is given in figure 2.1.

Photons are the carrier particles of the electromagnetic force, the Z- and W-Bosons carry the weak nuclear force and the run mediates the strong force. While quarks interact via all four forces, leptons are only affected by the weak force and gravity. Charged leptons additionally experience the electromagnetic force. For each particle, there exists an antiparticle with an inverted charge and in case of the strong interaction with the corresponding anticolor. All other properties remain the same.

Important for heavy-ion collisions is the strong interaction exchanged by gluons. The theory describing the strong force is called Quantum Chromodynamics (QCD). Quarks are bound together by constantly exchanging gluons. Both, quarks and gluons (also called partons), carry a so-called color charge. Gluons carry a color and the corresponding anticolor, while quarks always carry one color. A color and its anticolor as well as a combination of the three (anti-) colors add up to white. Observable systems build of quarks on gluons are always color neutral. The potential for this interaction is the phenomenological Cornell-Potential [Tho09]

$$V_{\text{QCD}}(r) = -\frac{4}{3}\frac{\alpha_s}{r} + \lambda r.$$

As one can see, the potential seen in figure 2.2 is a sum of a confining term proportional to the distance r between the particles and an attractive term proportional to $1/r$. The factor α_s is the strong coupling constant, which exact value depends on the distance between the two interacting particles and the energy. With increasing energy, the value of α_s decreases, and the interaction between the particles becomes asymptotically weaker.

Unlike the Quantum Electrodynamics (QED) potential $V_{\text{QED}} = -\alpha/r$ [Tho09], V_{QCD} does not converge asymptotically towards zero. Instead, the linear term results in a rising tension between the particles with an increment of $\lambda \approx 1\,\text{GeV}\,\text{fm}^{-1}$ [PPR83]. By pulling two color-charged particles further away, the energy between them increases. If enough energy is stored in this flux tube, new quark-antiquark pairs ($q\bar{q}$-pairs) are created. Thus, the quarks and gluons can never be observed independently. They are always bound together to form color-neutral particles. This phenomenon is called confinement.

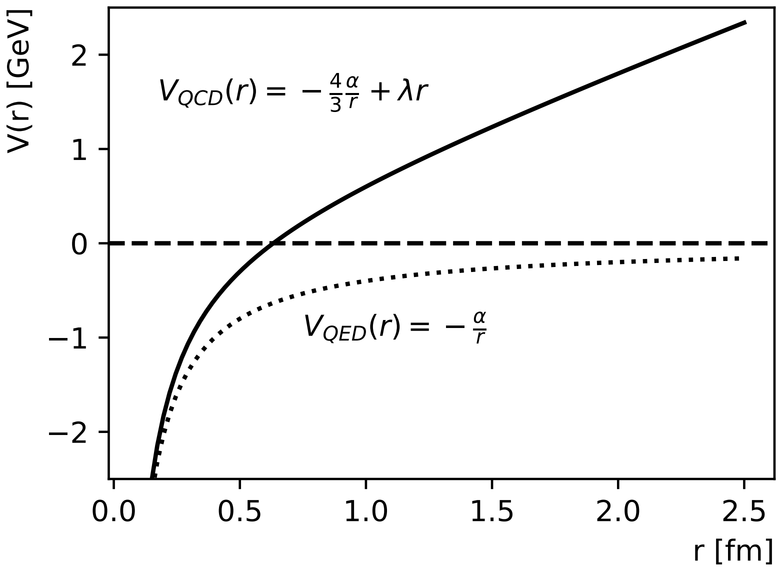

Figure 2.2: Comparison sketch of the QCD and QED potentials.

2.2 The Quark-Gluon Plasma

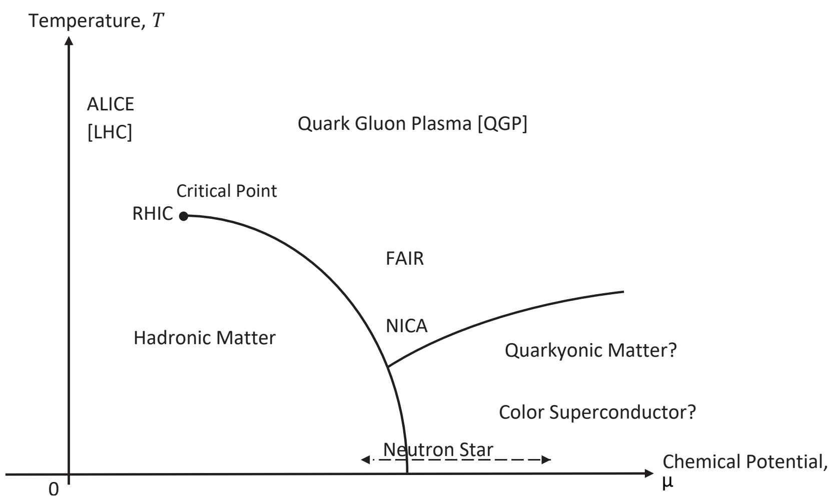

Figure 2.3: Phase diagram of the quark gluon plasma with important areas where different colliders operate at [McI16].

Under certain conditions, it is possible to break the confinement of quarks and gluons. If the nuclear matter is heated up above a critical temperature T_c, the partons show a quasi-free behavior. This state is called a Quark-Gluon Plasma (QPG) and is predicted by QCD [Ian14].

Figure 2.3 shows the possible phase diagram for the quark gluon plasma. In the early universe, the matter formed a QPG and about 10^{-5} s after the Big Bang the matter hadronized

[ABM04]. Today, in nature, a QGP could exist in the center of massive neutron stars, though this is still an open question [AGK+20]. In particle accelerators like the LHC at CERN, a QGP is formed in collisions of heavy nuclei. Since the QPG is an unstable system with a lifetime of less than 10 fm to 20 fm ($3-6\times10^{-23}$ s) [Str14], the medium itself cannot be observed, but its remnants show themselves in the detectors. Figure 2.4 shows a space-time-

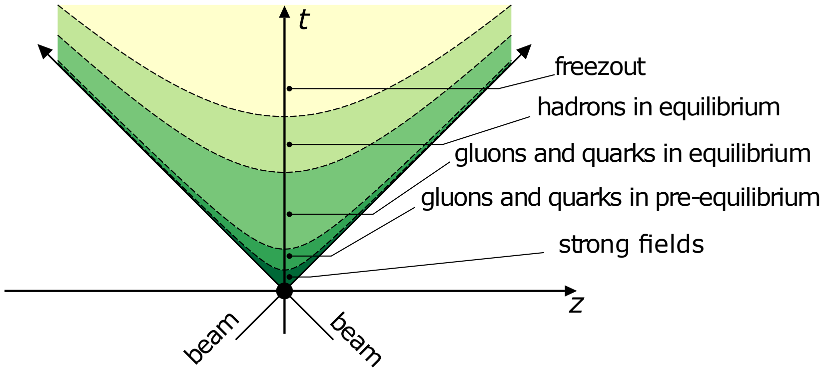

Figure 2.4: Space-time diagram of the evolution of QGP in a heavy-ion collision [Gro18].

diagram of the evolution of a heavy-ion collision. The collision occurs at $t=0$, the state reaches thermal equilibrium after $t\approx 1$ fm. Within that time, the system has expanded with a velocity near the speed of light. After the temperature dropped below T_c, the quarks and gluons form hadrons. The hadron gas expands further while the rate of ongoing inelastic collisions decreases until chemical freeze-out is reached.

2.3 Kinematic Variables

Heavy-Ion collisions are characterized through different kinematic variables [JS11]. The first important one to mention is the transverse momentum p_T. It is defined as the projection of the momentum on the plane perpendicular to the beam axis, which can be chosen as the z-axis, so that

$$p_\mathrm{T} = \sqrt{p_x^2 + p_y^2} = p\sin(\theta). \tag{2.1}$$

The angle θ is the polar angle between the beam axis and the particle and $p=|\vec{p}|$. Another important variable is the rapidity, which is an additive measure of the velocity of the particle and is defined by

$$y = \frac{1}{2}\ln\left(\frac{E+p_z}{E-p_z}\right) \tag{2.2}$$

where E is the energy and p_z is the momentum component parallel to the beam axis. In high energy physics, the rest mass of the particle is much smaller than the absolute value of the total momentum, which one can use to approximate $y\approx\eta$ with the pseudorapidity η, defined by $\eta = -\ln\left[\tan\left(\frac{\theta}{2}\right)\right]$. Furthermore, natural units are used throughout this thesis, so that $c = \hbar = 1$.

2.4 Glauber Model

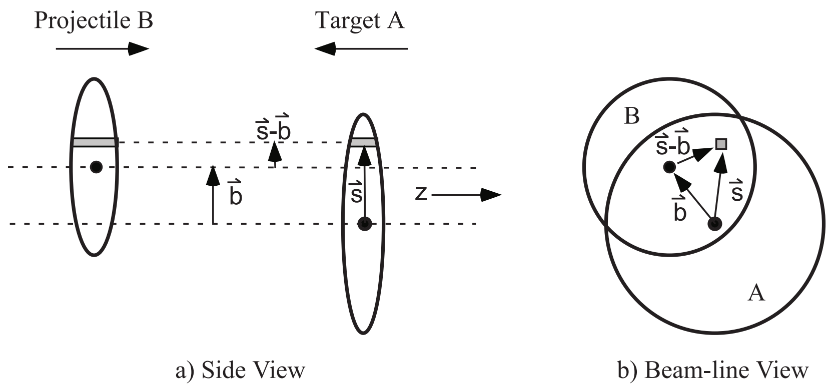

Figure 2.5: Schematic collision process of two nuclei A and B in the Glauber Model with Side View (a) and Beam-Line-View (b) [MRSS07].

The Glauber Model is used to simulate the geometry of heavy-ion collisions. Using this model, one can estimate the number of participating nucleons (N_{part}) and the number of binary nucleon-nucleon (NN) collisions (N_{coll}) in a collision process of a Projectile B and a Target A, which denote the mass numbers of the nuclei. The impact parameter b is defined as the distance of closest approach between the barycenter of the nuclei. Given the probability density $\rho_A(\vec{s}, z_A)$ of finding a nucleon per unit volume, one can calculate the probability $T_A(\vec{s})$ of finding a nucleon in an infinitesimal area displaced by $\vec{s}$ of the center of the nucleus by integration $T_A(\vec{s}) = \int \rho_A(\vec{s}, z_A)\,\mathrm{d}z_A$. For both nuclei, the integral $T_{AB}(\vec{b}) = \int T_A(\vec{s})T_B(\vec{s} - \vec{b})\,\mathrm{d}^2 s$ gives the nuclear thickness function. The probability of an interaction to happen is given by the product $\sigma_{\text{inel}}^{\text{NN}} \cdot T_{AB}(b)$ where $\sigma_{\text{inel}}^{\text{NN}}$ is the inelastic nucleus-nucleus cross-section. Given these quantities, one can calculate the number of nucleon-nucleon collisions as $N_{\text{coll}}(b) = AB \cdot T_{AB}(b) \cdot \sigma_{\text{inel}}^{\text{NN}}$. Figure 2.5 shows an example collision process in the Glauber model.

3 Experimental Observations in Heavy-Ion Collisions

In the following chapter, a short overview of the experimental observations made in heavy-ion collisions is given together with a brief description of the analyzed observables [Gro18]. The main focus lies on the production of charged particles. Throughout this thesis, protons, pions, kaons and their respective antiparticles are considered.

Production of charged particles The production of charged particles can be observed at different p_{T}. Hard processes, where the momentum transfer Q is substantial with respect to the QCD scale $Q > \Lambda_{\mathrm{QCD}}$, play a crucial role at high p_{T}, while at low values, soft probes have the highest impact on the production of charged particles. The soft probes can provide information about the medium created before. The hard probes are thought to correlate with N_{coll} while the soft probes are assumed to scale with N_{part}. The dependence of the production of the collision energy $\sqrt{s_{\mathrm{NN}}}$ is described by a power law with a bigger exponent for Pb-Pb collisions compared to pp. This indicates that the collisions of heavy nuclei are not just a sum of independent pp collisions.

Spectra of charged particles and the Nuclear Modification Factor The charged particle multiplicity $\mathrm{d}N/\mathrm{d}N_{\mathrm{ch}}$ (or $P(N_{\mathrm{ch}})$) gives the probability of finding a specific number of charged particles in an event. In different types of collisions, the mean transverse momentum has a dependency on the multiplicity.
With the transverse-momentum spectra $\mathrm{d}^2N_{\mathrm{ch}}/\mathrm{d}p_{\mathrm{T}}\mathrm{d}\eta$, one can determine the number of particles with a certain p_{T}value in the given pseudorapidity interval η. Additionally, it allows an insight to the modification of the charged particles through the QPG medium. A common observable to quantize those modifications is the Nuclear Modification Factor

$$R_{\mathrm{AA}}(p_{\mathrm{T}}) = \frac{1}{\langle N_{\mathrm{coll}} \rangle} \frac{\mathrm{d}^2 N_{\mathrm{ch}}^{\mathrm{AA}} \,/\, \mathrm{d}\eta \, \mathrm{d}p_{\mathrm{T}}}{\mathrm{d}^2 N_{\mathrm{ch}}^{\mathrm{pp}} \,/\, \mathrm{d}\eta \, \mathrm{d}p_{\mathrm{T}}}. \tag{3.1}$$

$N_{\mathrm{ch}}^{\mathrm{AA}}$ is the multiplicity of charged particles in nucleus-nucleaus (AA) collisions while $N_{\mathrm{ch}}^{\mathrm{pp}}$ is in a proton-proton collision. The ratio is scaled by $1/\langle N_{\mathrm{coll}} \rangle$. Hence, a factor of $R_{\mathrm{AA}} = 1$ implies that no modification to the medium happened, $R_{\mathrm{AA}} > 1$ means an enhanced particle yield and $R_{\mathrm{AA}} < 1$ indicates a suppression of the charged particle yield. Without any modifications through the medium, the AA spectrum is expected to be an independent sum of pp collisions [Col18].

Multiplicity dependence of mean transverse momentum The charged-particle production can be quantified by the observation of the mean transverse momentum $\langle p_{\mathrm{T}} \rangle$ of a collision as a function of the number of charged particles N_{ch}. It is observed, that $\langle p_{\mathrm{T}} \rangle$ monotonically increases with a rising number of particles. This indicates a collective expansion in pp collisions [Col22]. If the produced particles were fully independent, the mean transverse momentum would show a constant increase with the number of particles. For Lead-Lead collisions, a weaker dependency of N_{ch} is observed. In asymmetric p-Pb, collisions a similar increase like in pp collisions is observed, while the dependency decreases with higher N_{ch} too.

4 Experimental Setup

In this chapter, the experimental setup of the measured datasets used is described. All measurements were performed with the ALICE detector, located in France. ALICE is one of the largest experiments at the LHC, which is operated by CERN. An overview of the LHC with the ALICE detector and its subdetectors is provided, as well as the sources for each measured dataset.

4.1 The Large Hadron Collider

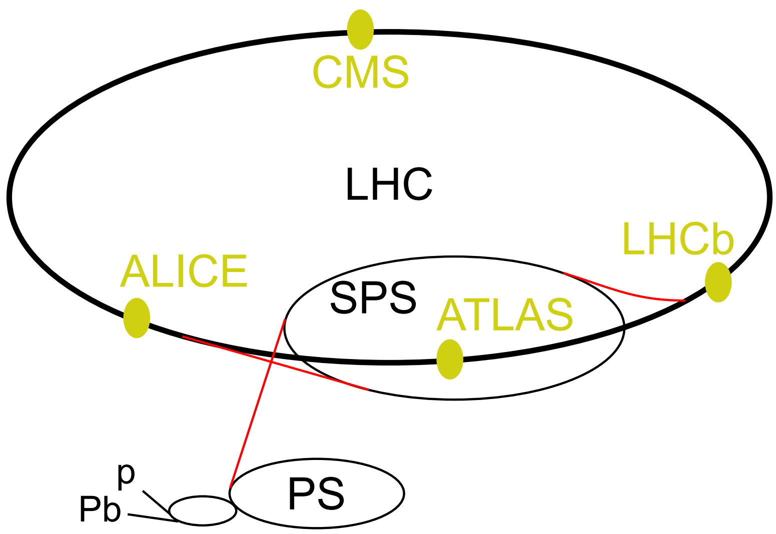

Figure 4.1: View of the CERN accelerator complex. Shown are the Large Hadron Collider (LHC), the pre-accelerators and the four intersection points with the main experiments [Mob16].

The Large Hadron Collider (LHC) is currently the largest particle collider in the world, located in Switzerland and France [EG21]. It consists of a 27 km long tunnel with several pre-accelerators to collide protons and lead ions. The LHC itself is a synchrotron with two beam pipes directed in opposite directions. It can reach up to 6.5 TeV of kinetic energy per proton and thus a center-of-mass energy $\sqrt{s} = 13\,\mathrm{TeV}$ per proton pair. For lead ions, the center-of-mass energy per nucleon pair is $\sqrt{s_{\mathrm{NN}}} = 5.02\,\mathrm{TeV}$. The beam pipes intersect at four points around the tunnel. Around each of these points, one of the experiments ALICE (A Large Ion Collider Experiment), ATLAS (A Toroidal LHC ApparatuS), CMS (Compact Muon Solenoid), and LHCb (LHC beauty) are located. Near the CMS, ATLAS, and LHCb experiments, three smaller experiments are located: TOTEM at CMS, LHCf near ATLAS, and MoEDAL at the LHCb detector. An overview of the accelerator complex is shown in figure 4.1 [EG21]. Until today, there were two full data-taking periods run 1 (2010 to 2013) and run 2 (2015 to 2018) with run 3 (2022 to 2025) currently proceeding.

4.2 ALICE

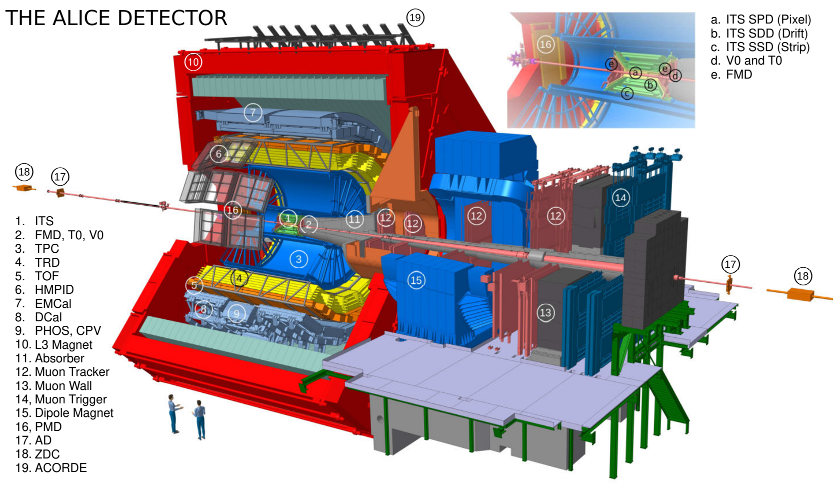

Figure 4.2: Schematic view of the run 2 ALICE detector with each subdetector numbered. The Inner Tracking System is described additionally in the upper right corner [Tau17].

The ALICE (A Large Ion Collider Experiment) detector is designed for the study of quark-gluon plasma created in collisions of lead nuclei [Col08]. In figure 4.2, a schematic overview of the detector is given. The beam pipe is surrounded by different layers of subdetectors for particle identification and tracking. Each subdetector lies concentrically around the beam pipe with the *Inner Tracking System* (ITS, (1)) in the innermost layer, followed by the *Time Projection Chamber* (TPC, (3)), the *Transition Radiation Detector* (TRD, (4)), and the *Time of Flight* (TOF, (5)) detector. They are mounted inside a large solenoid, capable of generating a magnetic field of $0.5\,\mathrm{T}$ and cover a full azimuthal range of $360°$. As seen in figure 4.2, there are more detectors placed around the beam axis, like calorimeters and spectrometers. Beside the ITS, there are the Forward Multiplicity Detector (FMD), T0 and V0 detectors which are used for event triggering and centrality determination in case of heavy-ion collisions.

4.3 Subdetector Systems

This section describes the subdetector systems of ALICE during run 2 in detail. They are used to obtain the measurements of the transverse-momentum distributions, the pseudorapidity distributions, the charged-particle multiplicity and the multiplicity dependence of the mean transverse momentum.

Inner Tracking System The Inner Tracking System is the most central detector, directly covering the beam pipe [Col14]. It consists of six layers of different types of silicon detectors. The two innermost layers are Silicon Pixel Detectors (SPD) which are followed by two Silicon Drift Detectors (SDD) and closes with two Silicon Strip Detectors (SSD). The purpose of the ITS is the localization of the primary vertex with a resolution of 100 µm, the reconstruction of secondary vertices from hyperon and D and B meson decays as well as the tracking and identification of particles with a momentum below 200 MeV and to improve the momentum and angular resolution for particles that were reconstructed by the TPC.
While the SPD only produces a binary signal for particle tracking, the SSD and SDD can be used for particle identification through the measurement of the energy loss $\mathrm{d}E/\mathrm{d}x$. The tracking covers a rapidity range of $|\eta| < 0.9$.

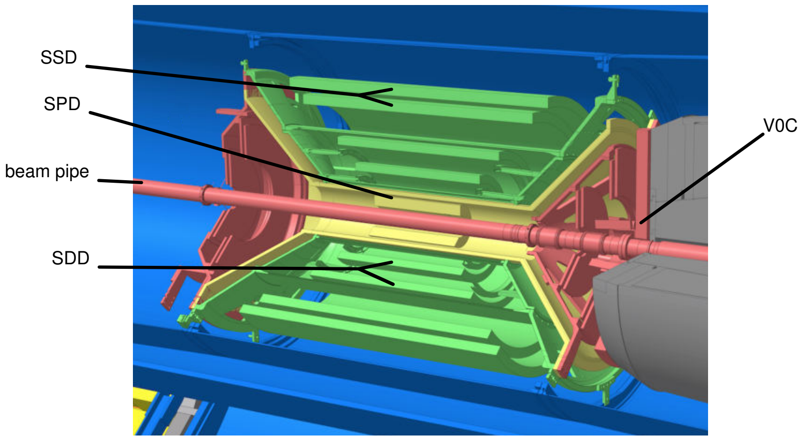

Figure 4.3: Schematic View of the Inner Tracking System. [Gro18]

Time Projection Chamber The Time Projection Chamber is the main subdetector used for particle tracking and identification [Col13b]. The detector is a cylindrical structure built around the ITS and is filled with a gas that is ionized by particles traversing the TPC volume. During run 1 and the late run 2, the gas mixture was made up of 90 parts Ne, ten parts CO_2 and five parts N_2. The cylinder is divided by a large central electrode which generates an electric field that is homogenized. The electrons produced in the ionization move through the electric field to the ends of the cylinder where the readout chambers are placed. The end plates are made of 18 trapezoidal sectors, each covering 20° of azimuthal range.

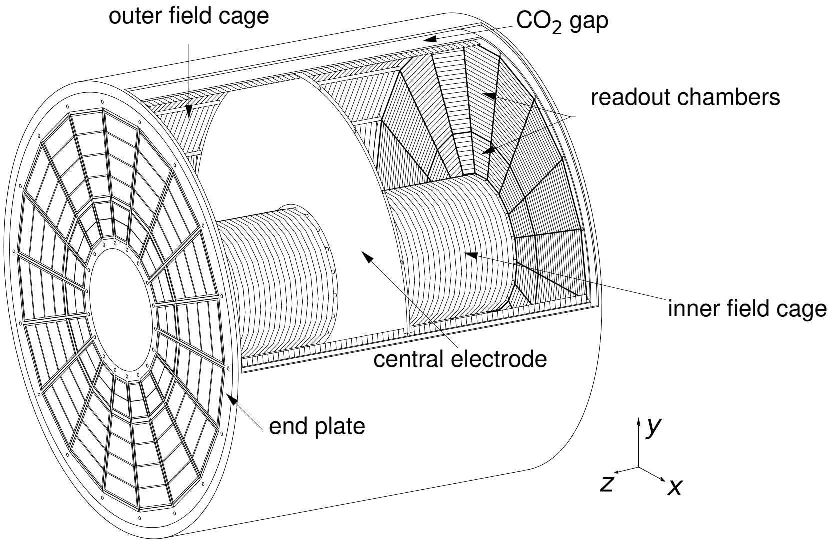

Figure 4.4: Schematic view of the Time Projection Chamber (TPC) [Col10].

ZDC, V0 and FMD Detectors The Zero-Degree Calorimeter (ZDC) is used to measure the energy of spectator nucleons and provides timing information [GKL$^+$99]. Placed near the ITS are the VZERO (V0) detectors V0A and V0C, which are mainly used for event triggering and the determination of the collision centrality [Col04]. The detector is made of two plates of plastic scintillators which are divided into eight segments in azimuth and four radial rings. Photomultipliers are used to read out the scintillator signals. The V0C detector covers a pseudorapidity range of $-3.7 < \eta < -1.7$ and the V0A detector covers a range from $2.8 < \eta < 5.1$.
The Forward Multiplicity Detector (FMD) is a silicon strip detector and provides high resolution multiplicity determination in a pseudorapidity range of $-3.4 < \eta < 5.1$ [Col07].

4.4 Datasets

The ALICE collaboration offers different kinds of datasets that were used for comparison in this thesis. The transverse-momentum distribution and the nuclear modification factors were analyzed with run 2 data and have been published 2018 in [Gro18, Col18]. Pseudorapidity distributions can be found in [Col23] and were published in 2023. A report of the charged particle multiplicity and the dependence of the mean transverse momentum of N_{ch} is given in [Col22] and was published in 2022.

5 EPOS4 Monte-Carlo Event Generator

The use of simulations has always been an important part in solving complicated problems in physics. For many applications based on statistical models, it is necessary to employ Monte-Carlo (MC) methods. Especially in high-energy physics, many problems cannot be calculated with perturbation theory because of the large coupling constant at low energy values and must be tackled with a Monte-Carlo approach. The collision of heavy ions is one such problem. During the collision process, particles are created. A MC event generator uses a theoretical model that describes the collision process. There are many models that are implemented in different event generators, e.g., Pythia, HIJING, or EPOS. In this thesis, the EPOS4 Monte-Carlo event generator is used to simulate heavy-ion collisions [Wer22]. The following chapter will describe the physics model behind the software and the usage of it. This description follows the introductions given in [Wer23b, Wer23a]. Afterwards, the used simulation setup is explained.

5.1 The EPOS Model

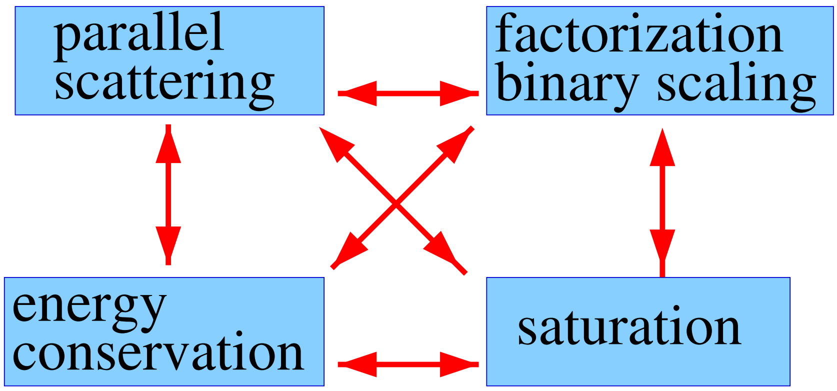

Figure 5.1: Schematic description of the four concepts used in the EPOS model [Wer23b].

The EPOS model is based on four basic concepts: **E**nergy conservation, **P**arallel scattering, fact**O**rization and **S**aturation [Wer23b]. Parallel scattering refers to the parallel nature of parton-parton scattering. Factorization means, that at some “factorization scale μ”, the scattering of two nuclei consisting of A and B nucleons can be *binary scaled* to $A \cdot B$ times the pp cross-section. In case of high-energy scatterings, partons with small Bjorken scale $x \ll 1$ become more and more important due to the fact that the parton distribution function become large at that scale, this is called *saturation*. Even though these concepts are important, a full theoretical treatment must include energy conservation.

EPOS4 uses a S-matrix approach to accommodate all four concepts. The S-Matrix is defined as $S_{fi} = \langle i|\hat{S}|f\rangle$ with a scattering Operator $\hat{S}$. The corresponding T matrix is defined via $S_{fi} = \delta_{fi} + i(2\pi)^4\delta(p_f - p_i)T_{fi}$. Assuming a full p_T transfer in the scattering process, one can write the Fourier transform of the T-Matrix as a sum of elementary T-Matrices, called T_pom, which represent parton-parton scattering by exchanging a Pomeron. This can be generalized to a product of pp collisions, to result in

$$iT = \int \mathrm{d}X \prod_{i=1}^{A} V \prod_{k=1}^{AB} \left\{ \sum_{n_k=0}^{\infty} \frac{1}{n_k!} \{iT_\mathrm{pom} \times \ldots \times iT_\mathrm{pom}\} \right\} \prod_{j=1}^{B} V. \tag{5.1}$$

The Vertex V represents the connection to the projectile and target remnants. The integration is done over all light-cone momentum fractions and all transverse positions of the nucleons. The connection to inelastic scattering processes is now given via the optical theorem [Sch13]. The total cross-section σ_tot of the process is then given by

$$2s\sigma_\mathrm{tot} = \frac{1}{i}\mathrm{disc}\,T \equiv \mathrm{cut}\,T \tag{5.2}$$

where $\mathrm{disc}\,T = T(s + i\epsilon) - T(s - i\epsilon)$ refers to the s-channel discontinuity. So, simulating pp, pA or AA, collision in the EPOS framework means to calculate the cut Pomeron $-i \cdot \mathrm{disc}(T_\mathrm{pom}) = G = G(x^+, x^-, s, b)$ with the light-cone momentum fractions $x^\pm$ and the impact parameter b. For each cut Pomeron the following equality is postulated

$$G(x^+, x^-, s, b) = \frac{n}{R_\mathrm{deform}(x_\mathrm{PE})} G_\mathrm{QCD}(Q^2_\mathrm{sat}, x^+, x^-, s, b). \tag{5.3}$$

Here, n is a normalization constant that does not depend on the $x^\pm$. The *deformation function* $R_\mathrm{deform} = f^{(N_\mathrm{conn})}(x_\mathrm{PE})/f^{(1)}(x_\mathrm{PE})$ quantifies the deformation of the "Pomeron energy fraction" $x_\mathrm{PE} = x^+x^-$ distributions $f(x_\mathrm{PE})$. $N_\mathrm{conn} = (N_\mathrm{P} + N_\mathrm{T})/2$ is the *connection number* which is half of the sum of the Pomerons connected to the projectile N_P and target nucleon N_T. G_QCD corresponds to a cut parton ladder based on the DGLAP parton evolutions [Tho13]. The DGLAP equations describe the dependency of the parton density function of the energy scale. Q^2_sat in this scale represents a dynamical saturation scale that "absorbs" the deformation. A more detailed description of this approach can be found in [Wer23b].

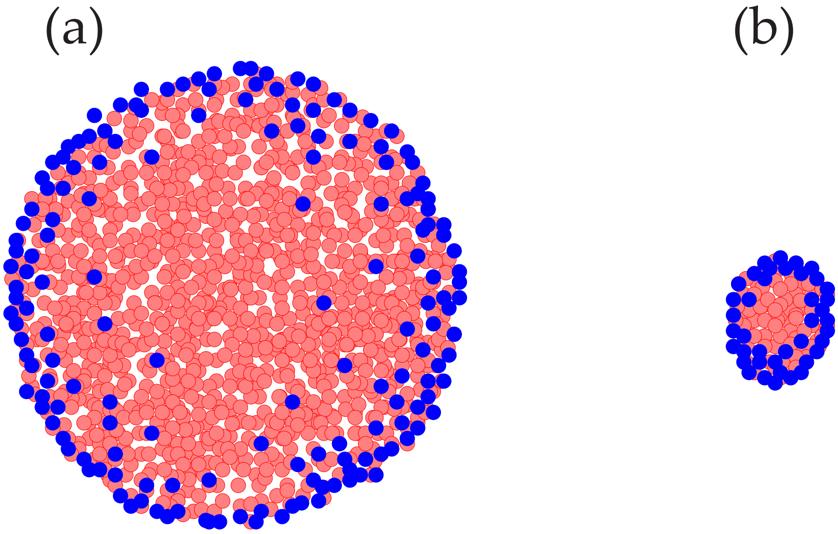

Figure 5.2: Schematic view of the core-corona separation for two systems of different size. The dots refer to prehadrons in the transverse plane. Red dots are part of the core, blue are part of the corona [Wer23a].

During a collision in EPOS, the particles produced first are so-called *prehadrons*, which hold the same quantum numbers as hadrons but do not need to be in a final state. They originate either from Pomerons or remnants of the target or projectile. Using these prehadrons as a foundation, one can identify a "core" and a "corona" part of the collision. The core holds a much higher energy density as the peripheral corona and can be treated as a fluid that evolves and possibly decays into hadrons that can collide with each other. The division of prehadrons into the core or into the corona is done via their energy loss. If the energy loss is bigger than the energy of the prehadron, it is marked as a core particle, otherwise it is a corona prehadron. The core is treated via hydrodynamics while the corona prehadrons simply become hadrons. The latter one is treated via microcanonical hadronization. The core-corona separation is introduced in [Wer07] with an update in [WGKP14].

5.2 Simulation Setup

To run a simulation with EPOS4, one must set up a so-called *options file*. In this file, all necessary parameters are set. The full options file used for the simulations in this thesis can be viewed in the appendix A.
In any simulation, the parameter *application* is set to *hadron* which includes hadron-hadron, hadron-nucleus and nucleus-nucleus scattering. Depending on which type of collision shall be simulated, projectile and target atomic and mass numbers can be specified. For a Proton, both are one. If either the projectile or target is a lead nucleus, the atomic number is 82 and the mass number is 208. The collision energy *ecms* is set to 5020 (in GeV).

The simulation in EPOS has different components. Those are: the *core*, the hydrodynamical evolution *hydro*, the equation of state *eos* and the hadronic cascade *hacas*. In this thesis, the hydrodynamical evolution is mimicked by using a *parameterized fluid expansion* (PFE) which increases the simulation speed. The parameter *core* is set to *PFE*. *hydro*, *eos* and *hacas* are set to *off*.
The number of simulated events can be set via *nfull* and is set to 1 000 000 for pp and p-Pb collisions and 100 000 for Pb-Pb collisions. The number of freezeout events per hydro evolution *nfreeze* is set to 1, a value greater than that only has an impact in case of a full simulation which also holds for the parameter *ninicon*, the number of initial conditions. Moreover, it is possible to set a specific collision *centrality*, which means the impact parameter of the collision. This is set to 0 to simulate minimum bias events. The output of the simulation must be printed with the command *fillTree4(C1)* which produces a ROOT file. The parameter *C1* sets the impact parameter as the centrality variable (a value of *C2* would use the number of Pomerons).

6 Data Analysis

In this thesis, different spectra of proton–proton, proton–lead, and lead-lead collisions at a center-of-mass energy of 5.02 TeV are analyzed. For pp and p-Pb, a total number of 10^6 events are simulated, for Pb-Pb only 10^5 events are simulated because of the long simulation time of about 2 weeks and the necessary storage amount. All measured datasets and simulations were filtered using the minimum-bias (MB) trigger. For Pb-Pb collisions, the analysis is also performed for nine classes of centrality. The ROOT data analysis framework published by CERN is used to analyze the data [CER]. Each spectrum is compared to datasets measured with the ALICE detector at the same collision energy in a pseudorapidity interval of $|\eta| < 0.8$, except the pseudorapidity distributions, which are measured in an interval of $-3.5 < \eta < 5$. All ALICE datasets provide statistical uncertainties σ_{stat} and systematic uncertainties σ_{sys}. Both are shown separately in the figures. Statistical uncertainties are marked with error bars while systematic uncertainties are displayed as boxes around the value. With x_{MC} being the bin-value of the simulated distribution and x_{Data} the bin-value of the ALICE datasets, the ratios are calculated by $r = x_{\mathrm{Data}}/x_{\mathrm{MC}}$ with uncorrelated uncertainties. Statistical and systematic uncertainties of the data are added in quadrature $\sigma_{\mathrm{tot}} = \sqrt{\sigma_{\mathrm{stat}}^2 + \sigma_{\mathrm{sys}}^2}$ that leads to a total uncertainty for ratios of

$$\sigma_{\mathrm{ratio}} = \sqrt{\left(\frac{\sigma_{\mathrm{tot}}}{x_{\mathrm{MC}}}\right)^2 + \left(\frac{x_{\mathrm{Data}}}{x_{\mathrm{MC}}^2}\sigma_{\mathrm{MC}}\right)^2} \tag{6.1}$$

according to the Gaussian formula for the propagation of uncorrelated uncertainties.
Each observable is shown together with the corresponding ALICE dataset and the ratios of the spectra in one canvas. Simulation results and data are shown in the upper half, and the ratio is shown in the lower half of the canvas. The binning of the EPOS4 data is adapted from the ALICE datasets to ensure comparability.

6.1 Results for Proton-Proton Collisions

The first setup discussed is the collision of two protons. A transverse-momentum distribution is shown and analyzed, followed by the pseudorapidity distribution. Next, the charged-particle multiplicity is reviewed, and the multiplicity dependence of the mean transverse momentum is discussed.

Transverse-Momentum Distribution

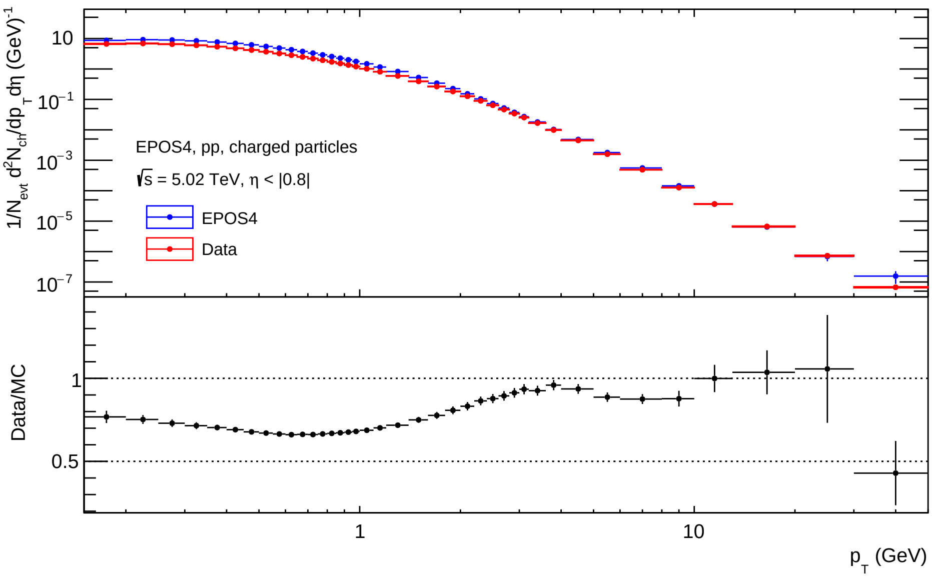

Figure 6.1: Transverse-Momentum Distribution of charged particles in pp collisions at $\sqrt{s} = 5.02\,\text{TeV}$ in a pseudorapidity interval of $\eta < |0.8|$. Both axes are logarithmic. The distribution is compared to data from the ALICE experiment.

The transverse-momentum distribution of pp collisions at $\sqrt{s} = 5.02\,\text{TeV}$ is shown in figure 6.1. In the $p_\mathrm{T} < 10\,\text{GeV}$ region, the simulation overestimates the data and does not reach unity at any point within the uncertainty interval. For 0.15 GeV to 3.6 GeV, the ratio has a valley with a minimum at 0.7 GeV and rises close to unity at 3.6 GeV. Between 3.6 GeV and 10.0 GeV, the simulation overestimates the multiplicity, leading to a drop in the ratio to about 0.85. The simulated distribution indicates a strong increase in uncertainties in the region above 10 GeV. This is due to the increase in the statistical uncertainties in the simulation because particles with high-p_T are less likely to be produced.

Pseudorapidity Distribution

Figure 6.2 displays the pseudorapidity distribution of pp collisions alongside the data from the ALICE experiment in a range of $-3.5 < \eta < 5$. EPOS4 is overestimating the pseudorapidity distribution over the full range by 54 to 60 percentage points. In the range of $-3.5 < \eta < 3$, the shape is well-preserved with fluctuations in the ratio of less than 1 percentage point. For $\eta > 3$, the ALICE data curve shows a steeper decrease than the EPOS4 curve and reaches a plateau, while as the EPOS4 distribution decreases further.

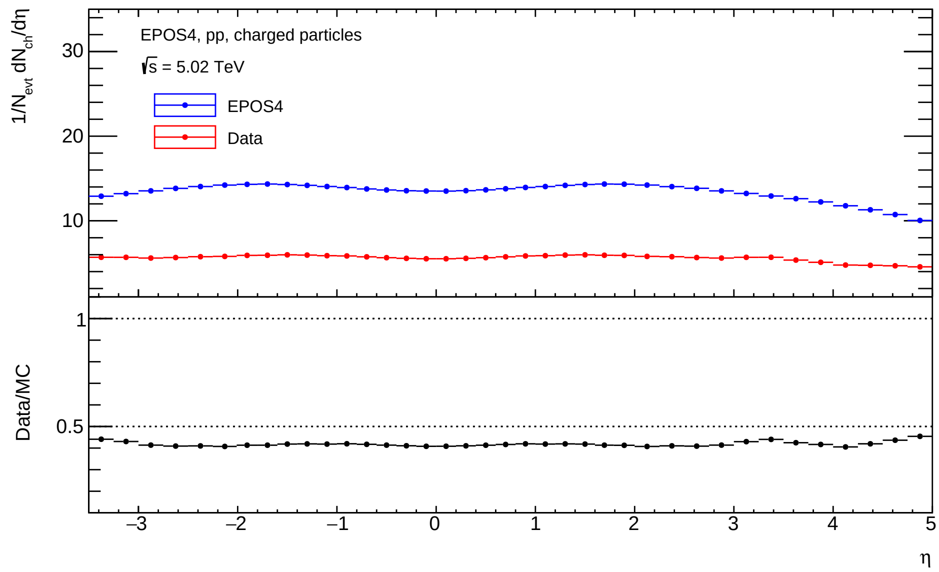

Figure 6.2: Pseudorapidity distribution of charged particles in pp collisions at $\sqrt{s} = 5.02\,\text{TeV}$. The distribution is compared to data from the ALICE experiment. Systematic and statistical uncertainties of the data are added in quadrature in this case.

Charged-Particle Multiplicity

In figure 6.3, the charged-particle multiplicity for pp collisions is shown. In the low-multiplicity regime of $N_{\text{ch}} < 6$, the ratio of the measured ALICE data and EPOS4 decreases by a difference of 80 percentage points to a plateau in the range of $N_{\text{ch}} \approx 6$ to 10 where it remains constant at 1 percentage point deviation. Above a multiplicity of 10 particles, the ALICE data curve is steeper than the EPOS4 curve, and both curves are separate.

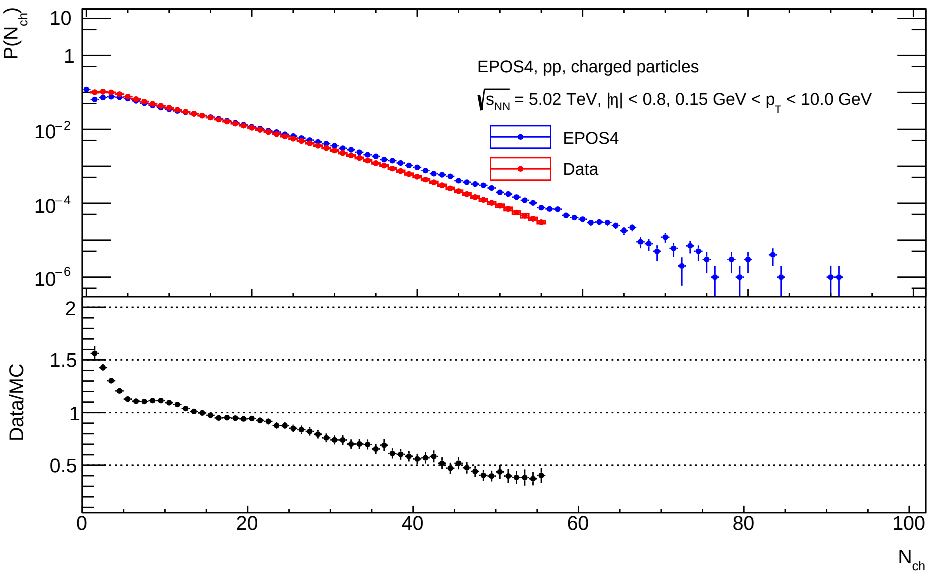

Figure 6.3: The charged-particle multiplicity in pp collisions at $\sqrt{s} = 5.02\,\mathrm{TeV}$ in an interval of $\eta < |0.8|$ and $0.15\,\mathrm{TeV} < p_\mathrm{T} < 10.0\,\mathrm{GeV}$. The y-axis is logarithmic. The multiplicity is compared to data from the ALICE experiment.

Multiplicity Dependence of $\langle p_\mathrm{T} \rangle$

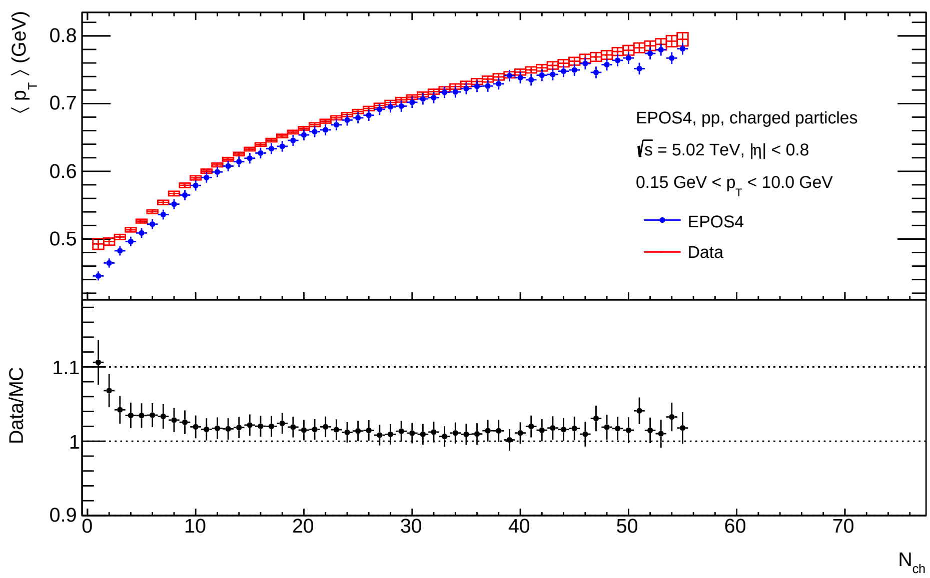

Figure 6.4: Multiplicity dependence of the mean transverse momentum of charged particles in pp collisions at $\sqrt{s} = 5.02\,\mathrm{TeV}$ in an interval of $\eta < |0.8|$ and $0.15\,\mathrm{TeV} < p_\mathrm{T} < 10.0\,\mathrm{GeV}$. The distribution is compared to data from the ALICE experiment.

The mean transverse momentum $\langle p_\mathrm{T} \rangle$ in the pp simulation as a function of the charged-particle multiplicity is portrayed in figure 6.4. The two shapes agree well for $N_\mathrm{ch} > 10$ and differ by only 1 to 2 percentage points. For $N_\mathrm{ch} < 10$, the EPOS4 curve begins at a lower $\langle p_\mathrm{T} \rangle$ value but rises steeper than the data curve. Both show a decrease in their slope at $N_\mathrm{ch} \approx 11$. The decrease is slightly different, which can be seen as an increase in the ratio between $10 < N_\mathrm{ch} < 20$.

6.2 Results for Proton-Lead Collisions

In the second setup, the target proton is replaced by a Pb_{208} nuclei. The same observables as in pp collisions are analyzed. For the p-Pb setup, no parameterized fluid expansion was available, hence the simulation was performed without this option.

Transverse-Momentum Distribution

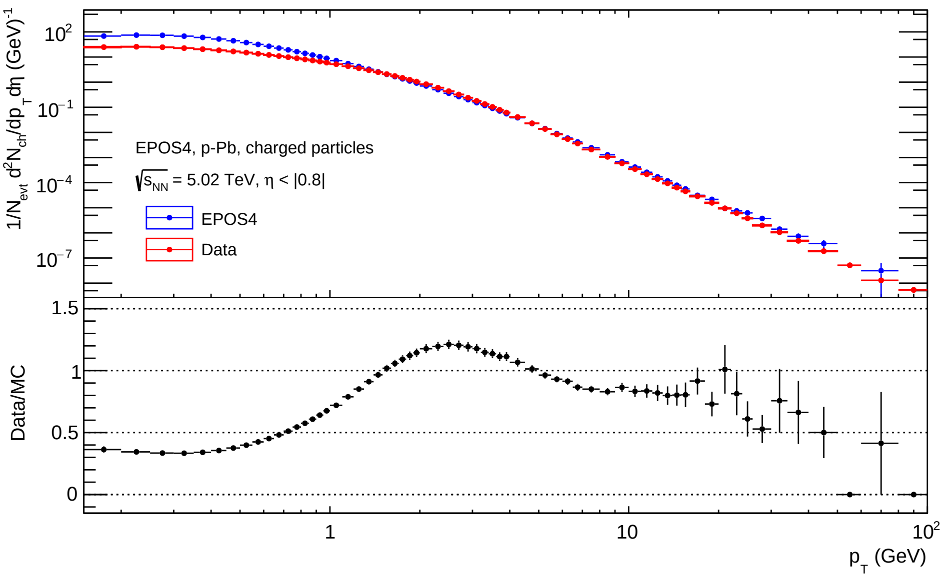

Figure 6.5: Transverse-Momentum Distribution of charged particles in p-Pb collisions at $\sqrt{s_\mathrm{NN}} = 5.02\,\mathrm{TeV}$ in a pseudorapidity interval of $\eta < |0.8|$. Both axes are logarithmic. The distribution is compared to data from the ALICE experiment. Systematic and statistical uncertainties of the data are added in quadrature in this case.

The transverse-momentum distribution for p-Pb collisions is shown in figure 6.5. In the low p_T region $< 0.6\,\mathrm{GeV}$, the distributions differ by 50 to 60 percentage points. In the $0.6\,\mathrm{GeV}$ to $2.5\,\mathrm{GeV}$ region, a steep increase up to a ratio of 1.2 can be observed, followed by a decrease to a plateau at 0.8 in the region from 8 GeV to 20 GeV. Above 20 GeV, the ratio fluctuates between 0 and 1 and increases in uncertainty. The 80 GeV and 100 GeV bins are empty, the ratio is therefore set to zero at this point. In comparison to the results from pp collisions, the p-Pb distribution has a greater deviation from the ALICE datasets, especially in the low p_{T} region.

Pseudorapidity Distribution

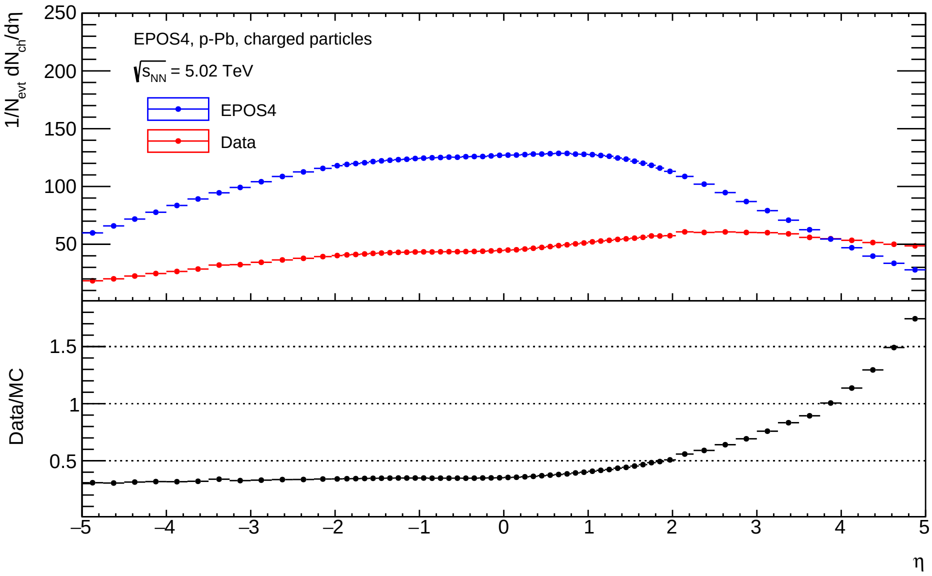

Figure 6.6: Pseudorapidity distribution of charged particles in p-Pb collisions with a centrality of 0 % to 5 % at $\sqrt{s_{\mathrm{NN}}} = 5.02\,\mathrm{TeV}$. The distribution is compared to data from the ALICE experiment.

The pseudorapidity distribution of p-Pb collisions in a centrality interval of 0 % to 5 % is portrayed in figure 6.7 and plotted in the interval $-5 < \eta < 5$. For this collision type, only the most central collisions are considered here because the pseudorapidity distribution is the only observable in the p-Pb case that is investigated within different centrality classes in this thesis. A definition of centrality and the determination of the intervals for the Pb-Pb case are given in section 6.4. The remaining classes are shown in Appendix A with a proper definition of the centrality in the p-Pb case.

In the $-5 < \eta < 0$ regime, the simulated curve shows a greater slope than the ALICE curve, resulting in a difference of 70 to 73 percentage points for $-5 < \eta < -2.5$ and 74 to 75 percentage points in the region $-2.5 < \eta < 0$, but the difference of the EPOS4 and ALICE dataset distributions remains within these ranges. Because of the asymmetry of the collision system, the distributions show a peak in the $\eta > 0$ region. The EPOS4 distribution has a peak at around $\eta \approx 1.5$, the ALICE data at $\eta \approx 2.5$. The shapes of both distributions also begin to differ more in the $\eta > 0$ region, resulting in an intersection of the distributions at $\eta \approx 4$.

Charged-Particle Multiplicity

The charged-particle multiplicity of p-Pb collisions is displayed in figure 6.7. In the regime $N_{\mathrm{ch}} < 55$, EPOS4 underestimates the data. After an initial increase up to a ratio of 2.9 at $N_{\mathrm{ch}} \approx 17$, where the EPOS4 curve falls into a valley, the simulation and the measured ALICE dataset approach each other. It decreases with a change in its slope at $N_{\mathrm{ch}} \approx 38$ and intersects with the data curve at $N_{\mathrm{ch}} = 55$. Both curves diverge from here on. Again, similar to pp collisions, EPOS4 does not preserve the shape of the charged-particle multiplicity.

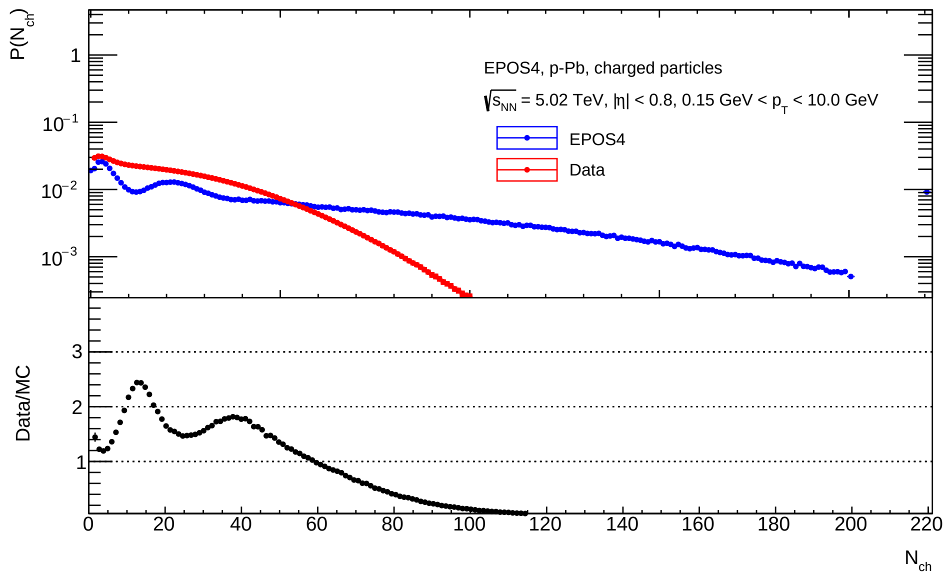

Figure 6.7: The charged-particle multiplicity in p-Pb collisions at $\sqrt{s_{\mathrm{NN}}} = 5.02\,\mathrm{TeV}$ in an interval of $\eta < |0.8|$ and $0.15\,\mathrm{TeV} < p_{\mathrm{T}} < 10.0\,\mathrm{GeV}$. The multiplicity is compared to data from the ALICE experiment.

Multiplicity Dependence of $\langle p_{\mathrm{T}} \rangle$

The dependence of the mean transverse momentum on the charged-particle multiplicity is shown in figure 6.8. The EPOS4 curve never intersects the data curve. After a peak at $N_{\mathrm{ch}} \approx 10$ up to $0.5\,\mathrm{GeV}$, it falls back to $0.4\,\mathrm{GeV}$ at $N_{\mathrm{ch}} \approx 20$. The curve increases monotonically for $N_{\mathrm{ch}} > 20$ with a slope different from that of the ALICE data curve, which can be seen by a small increase in the slope of the ratio in the region $N_{\mathrm{ch}} > 40$.

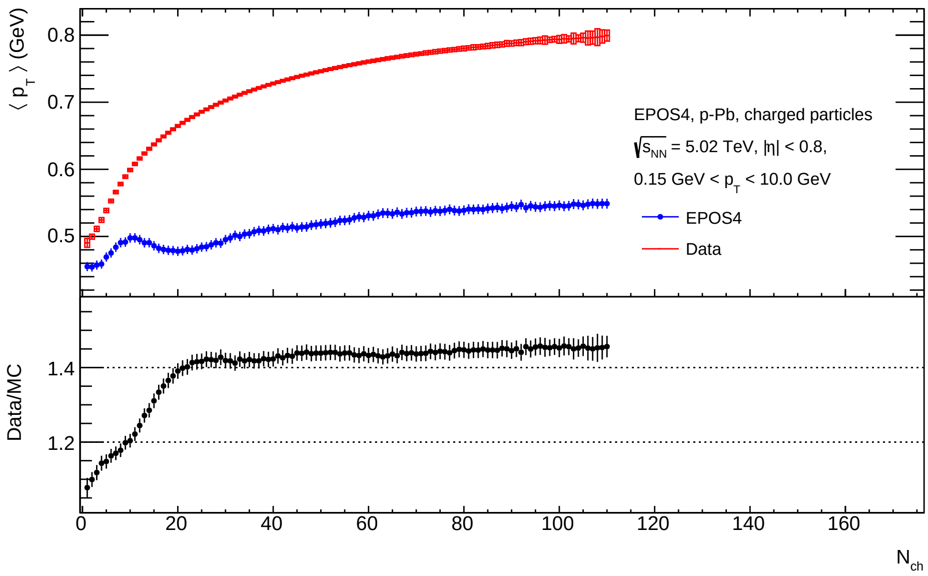

Figure 6.8: Multiplicity dependence of the mean transverse momentum of charged particles in p-Pb collisions at $\sqrt{s_{\mathrm{NN}}} = 5.02\,\mathrm{TeV}$ in an interval of $\eta < |0.8|$ and $0.15\,\mathrm{TeV} < p_{\mathrm{T}} < 10.0\,\mathrm{GeV}$. The distribution is compared to data from the ALICE experiment.

6.3 Results for Minimum-Bias Lead-Lead Collisions

The third setup deals with the collision of two Pb_{208} nucleis without any classification in the centrality classes. The same observables as in pp and p-Pb collisions are analyzed, except for the pseudorapidity distributions, which are discussed in chapter 6.4.

Transverse-Momentum Distribution

The transverse-momentum distributions for minimum-bias Pb-Pb collisions are shown in figure 6.9. Similar to pp and p-Pb collisions, EPOS4 overestimates the production of low-p_{T} charged particles up to $p_{\mathrm{T}} \approx 1.5\,\mathrm{GeV}$.
In the following p_{T} range of 1.5 GeV to 7 GeV, the ratio peaks at 4 GeV and reaches a value of 1.7. It drops into a valley with a minimum at 10 GeV and a ratio of 0.8. In the high-p_{T} region above 11 GeV, the distribution matches the data quite well, but with strongly increasing uncertainties.

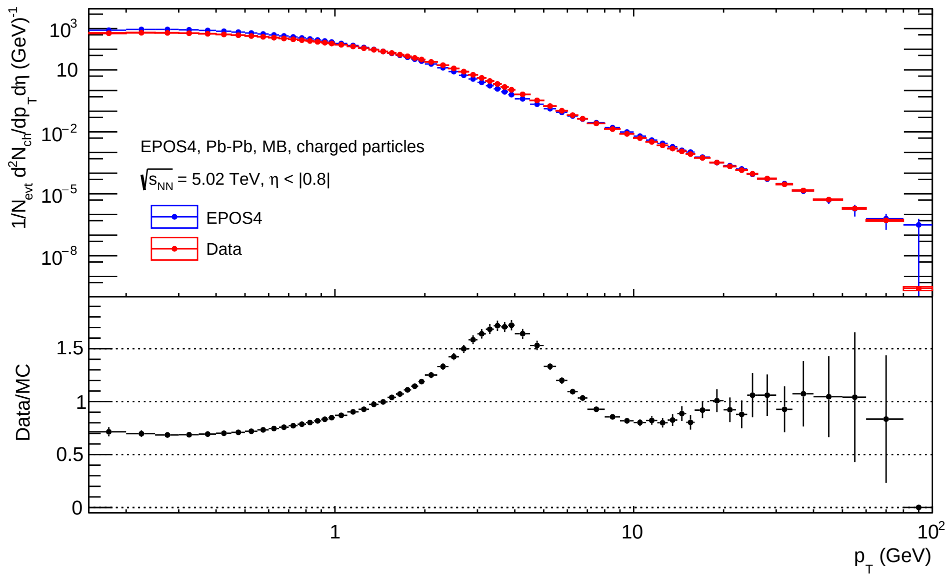

Figure 6.9: Transverse-Momentum Distribution of charged particles in Pb-Pb collisions at $\sqrt{s_{\mathrm{NN}}} = 5.02\,\mathrm{TeV}$ in a pseudorapidity interval of $\eta < |0.8|$. Both axes are logarithmic. The distribution is compared to data from the ALICE experiment.

Charged-Particle Multiplicity

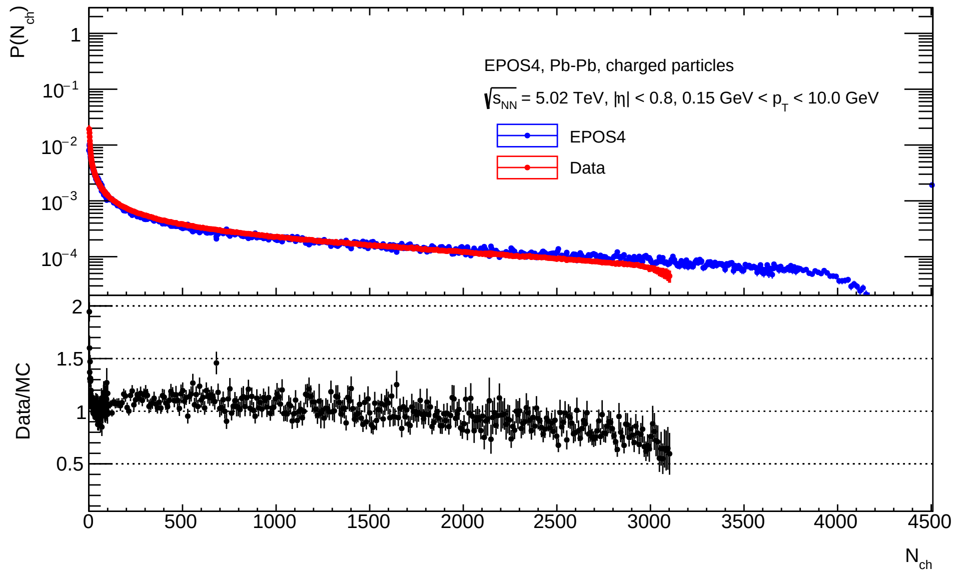

Figure 6.10: The charged-particle multiplicity in Pb-Pb collisions at $\sqrt{s_{\mathrm{NN}}} = 5.02\,\mathrm{TeV}$ in an interval of $\eta < |0.8|$ and $0.15\,\mathrm{TeV} < p_{\mathrm{T}} < 10.0\,\mathrm{GeV}$. The y-axis is logarithmic. The multiplicity is compared to data from the ALICE experiment. For better visibility, the ratio is rebinned by a factor of 4.

The charged-particle multiplicity is shown in figure 6.10. The EPOS4 curve matches the data curve well within a deviation of less than 20 percentage points. Up to $N_{\mathrm{ch}} \approx 1900$, EPOS4 overestimates the multiplicity and intersects with the data curve, which decreases steeper than the MC curve. The data curve also turns towards zero at $N_{\mathrm{ch}} \approx 3050$, a feature which EPOS4 does not reproduce at this point. Instead, the simulated curve decreases further and drops towards zero at a multiplicity of $N_{\mathrm{ch}} \approx 4150$. In comparison to pp and p-Pb collisions, the charged-particle multiplicity suddenly agrees very well with the ALICE data, beside the fact that the EPOS4 curve shows the drop towards zero at about 1000 particles further in the multiplicity.

Multiplicity Dependence of $\langle p_{\mathrm{T}} \rangle$

Figure 6.11 displays the multiplicity dependence of the mean transverse momentum in minimum-bias Pb-Pb collisions.
At a multiplicity below 5 particles, the curves deviate by less than 5 percentage points. The difference between both curves increases as the ALICE data curve, the data curve rises higher to a value of approximately 0.71 GeV while the EPOS4 curve remains at 0.62 GeV. Above a multiplicity of $N_{\mathrm{ch}} > 1500$ particles the fluctuations in the ratio are less than 1 percentage point, the shape of the simulated curve matches the ALICE data well in this regime. Also, the plateau is reached by a much lower multiplicity compared to the ALICE data.

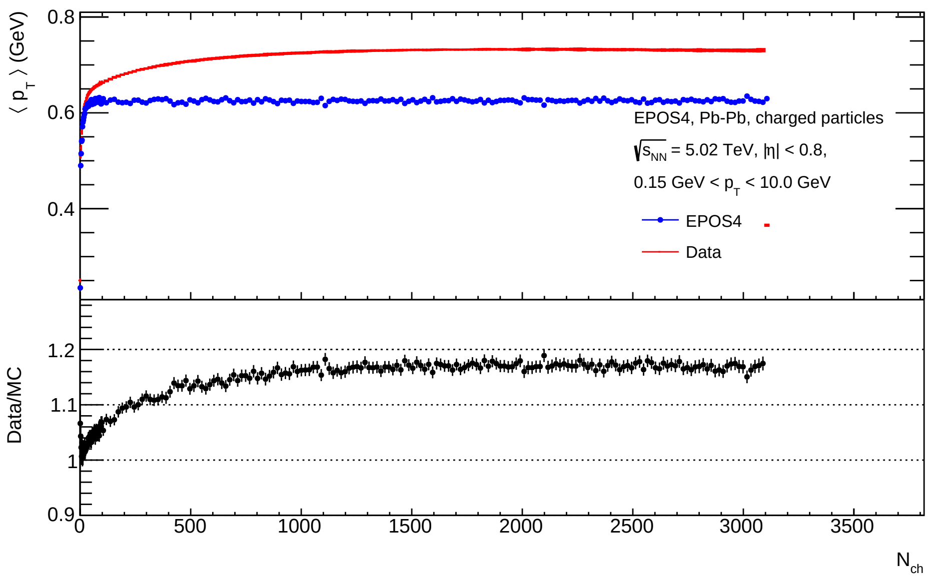

Figure 6.11: Multiplicity dependence of the mean transverse momentum of charged particles in Pb-Pb collisions at $\sqrt{s_{\mathrm{NN}}} = 5.02\,\mathrm{TeV}$ in an interval of $\eta < |0.8|$ and $0.15\,\mathrm{TeV} < p_{\mathrm{T}} < 10.0\,\mathrm{GeV}$. The distribution is compared to data from the ALICE experiment.

6.4 Results for Centrality-Sorted Lead-Lead Collisions

This section analyzes Pb-Pb collisions again, but now considers the different centrality classes of the collisions. First, the determination of the centrality classes in EPOS4 is described, followed by a discussion of the transverse-momentum distributions. In addition, nuclear modification factors and pseudorapidity distributions are shown for each interval.

Centrality Determination in EPOS4

The centrality of a collision is described as the percentage of the total geometric cross-section. Nine centrality intervals are defined where the events are sorted into, with the most central collision ranging from 0 % to 5 %.

Experimentally, the centrality of an event can be calculated by the charged-particle multiplicity in the V0 detectors. Each class corresponds to a range of impact parameters of the collision. The simulation output provides the impact parameter in an event, which is used to sort the event directly into a specific class. Table 6.1 lists the impact parameter range in EPOS4 for each centrality class, together with the mean number of binary collisions in the simulation, calculated using the Glauber model.

The impact parameter ranges together with the calculated data $\langle N_{\mathrm{coll}} \rangle$ can be found in [Col13a]. In the simulation output, a calculated N_{coll} is provided by EPOS4.

Table 6.1: Impact parameter range together with the corresponding centrality interval and the mean number of Glauber collisions for each class determined with EPOS4 in comparison to data.

Class	Centrality	b [fm]	$\langle N_{\mathrm{coll}} \rangle$ in EPOS4	$\langle N_{\mathrm{coll}} \rangle$ in Data
1	0 % to 5 %	0.0 to 3.48	1971.60 ± 0.58	1777 ± 59
2	5 % to 10 %	3.48 to 4.92	1531.19 ± 0.51	1389 ± 50
3	10 % to 20 %	4.92 to 6.96	1063.98 ± 0.60	973.4 ± 37.0
4	20 % to 30 %	6.69 to 8.51	633.92 ± 0.42	586.4 ± 20.0
5	30 % to 40 %	8.51 to 9.82	359.54 ± 0.29	336.7 ± 12.0
6	40 % to 50 %	9.82 to 10.99	188.98 ± 0.19	179.8 ± 7.1
7	50 % to 60 %	10.99 to 12.03	90.39 ± 0.11	88.22 ± 3.10
8	60 % to 70 %	12.03 to 12.99	39.47 ± 0.06	39.08 ± 1.60
9	70 % to 80 %	12.99 to 13.90	15.73 ± 0.03	15.57 ± 0.62

Transverse-Momentum Distributions

Figure 6.12 portrays the transverse-momentum distributions for each centrality class with the ALICE dataset. The related ratios are plotted in figure 6.13. An overview of the pp and p-Pb distributions can be found in the appendix A.3.

All classes behave similarly to the minimum-bias case. In the low-p_T region below 1.5 GeV, EPOS4 overestimates particle production but underestimates it between 1.5 GeV to 8 GeV. Especially around the turning point, EPOS4 produces fewer particles than in the ALICE experiment, creating a peak in the ratios. In the class 30 % to 40 %, the deviation reaches up to 90 percentage points. The simulated data overestimate particle production in the $p_\mathrm{T} > 8$ GeV area in each class. Above 10 GeV, each distribution shows high statistical uncertainties because of the small number of 10^4 events in each class.

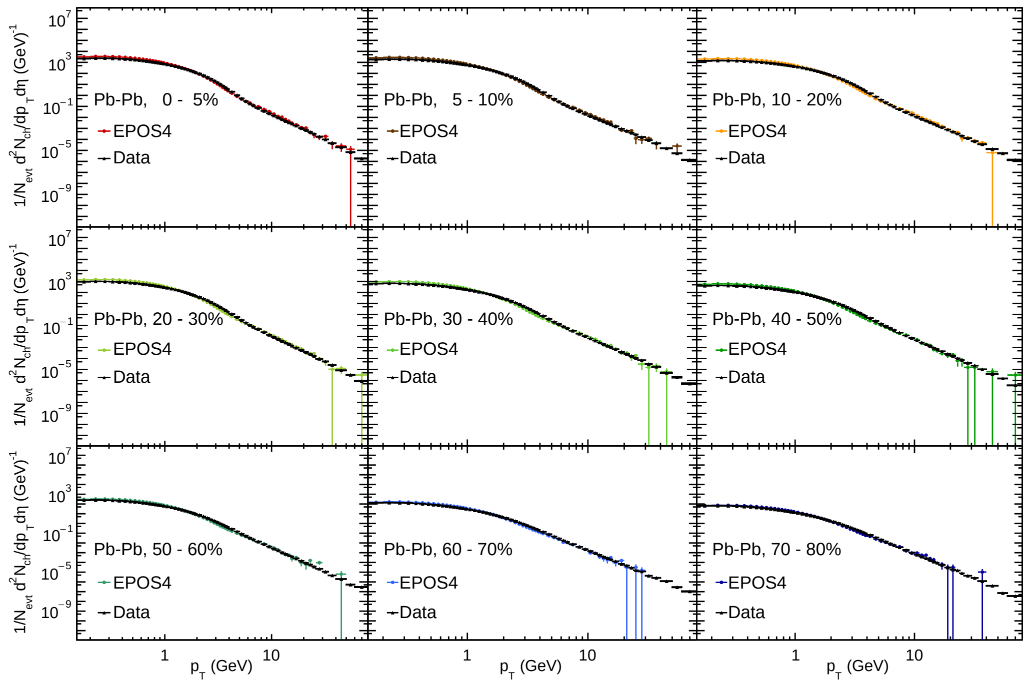

Figure 6.12: Transverse-Momentum Distribution of nine centrality classes of Pb-Pb collisions at $\sqrt{s_\mathrm{NN}} = 5.02$ TeV in a pseudorapidity interval of $\eta < |0.8|$. Both axes are logarithmic. The distributions are compared to data from the ALICE experiment.

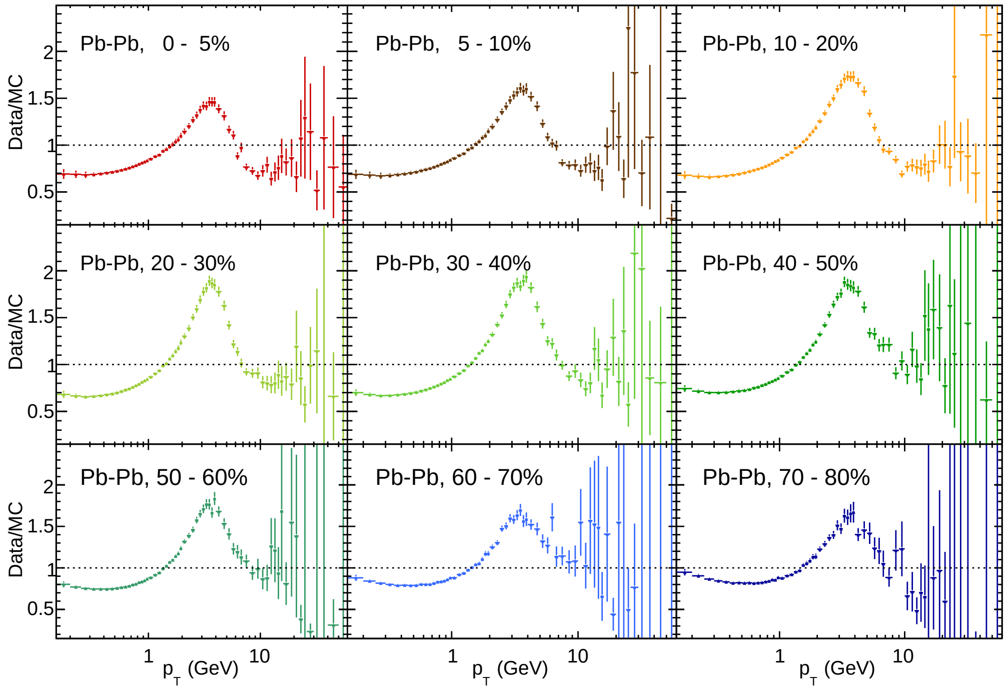

Figure 6.13: Ratios of transverse-momentum distributions of Pb-Pb collisions from figure 6.12.

Nuclear Modification Factors

The nuclear modification factors were calculated using equation 3.1 with the transverse-momentum distributions from chapter 6.1 for the pp reference and 6.4 for Pb-Pb. Figure 6.14 presents the calculated R_{PbPb} beside the measured ones, figure 6.15 displays the corresponding ratios of all nine centrality classes.

In each class, the simulation preserves the general shape of the nuclear modification factors, especially in the low p_{T} region below 0.7 GeV, but overestimates the medium modifications in the regions above 0.7 GeV, resulting in a smaller R_{PbPb} compared to the dataset. Each R_{PbPb} is below zero, except for some values in the high-p_{T} region in the three less central classes. Above 3 GeV, the simulation and the data approach each other again. In the high-p_{T} region > 10 GeV, the simulation and the data begin to overlap again within their uncertainty intervals, except for the last bin. This behavior is consistent with the transverse-momentum distributions in 6.1 and 6.12. The pp spectra show an overestimation of the ALICE datasets and the Pb-Pb spectra an underestimation in the same region. This results in lower R_{PbPb}, which implies an overestimation of the medium modifications by EPOS4. Overall, the agreement in the low-p_{T} regime increases with higher centrality. In the mid-p_{T} region, the deviation increases until a centrality of 30 % to 40 % is reached, where the EPOS4 and ALICE data approach each other again.

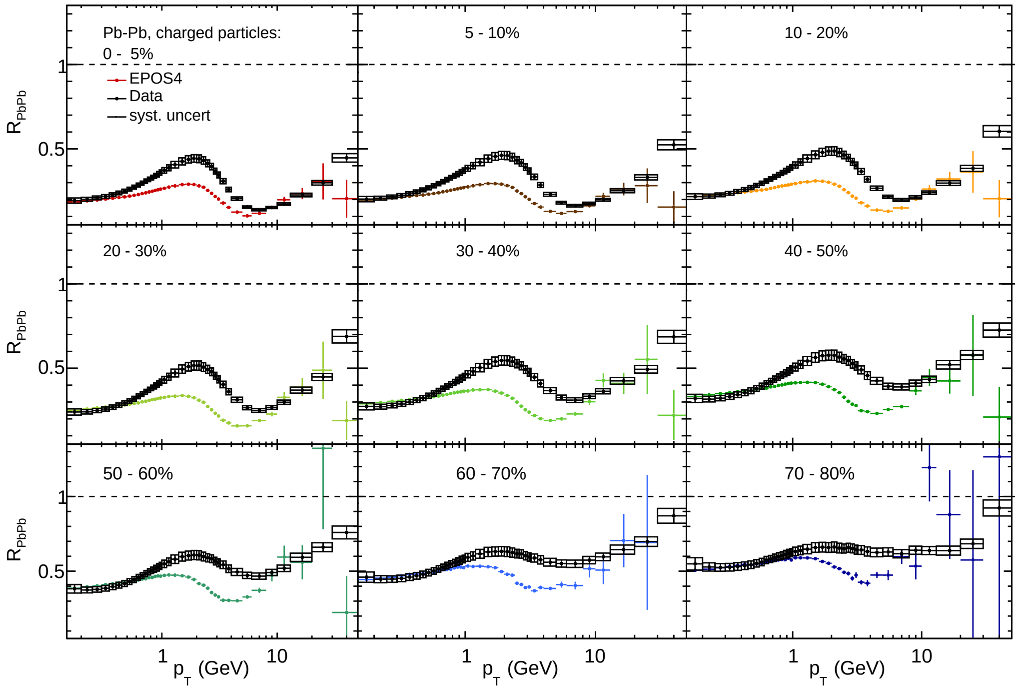

Figure 6.14: Nuclear modification factors in Pb-Pb collisions for nine centrality classes at $\sqrt{s_{\mathrm{NN}}} = 5.02\,\mathrm{TeV}$ in a pseudorapidity interval of $\eta < |0.8|$. The x-axis is logarithmic. The black curves are data measured by the ALICE experiment.

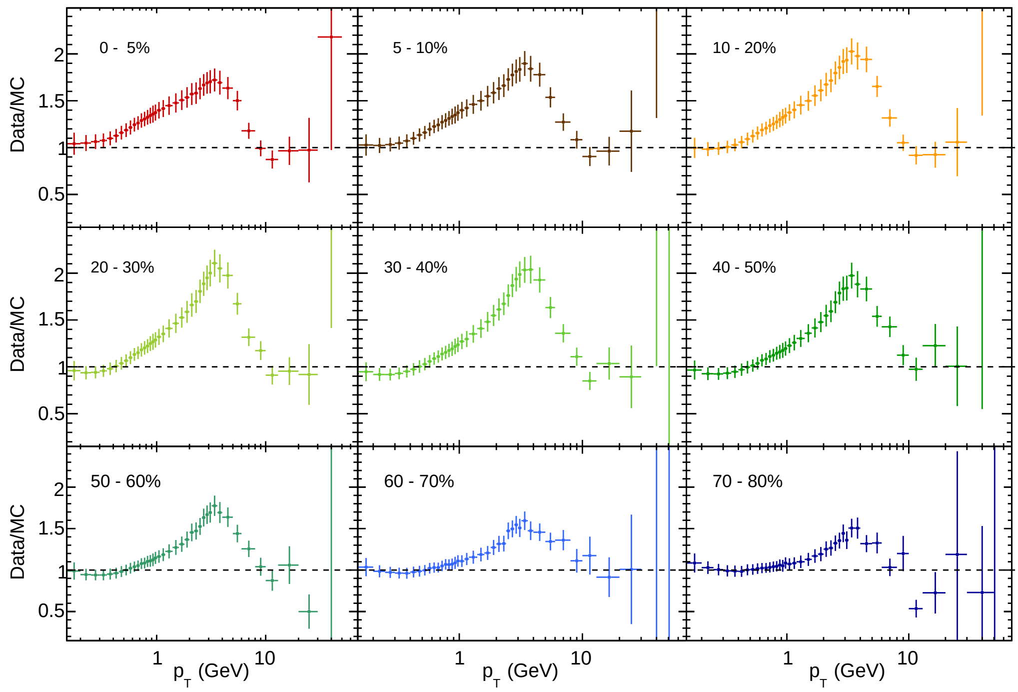

Figure 6.15: Ratios of nuclear modification factors calculated with EPOS4 in comparison to ALICE datasets.

Pseudorapidity Distributions

For each centrality class, the pseudorapidity distributions in the range from $-5 < \eta < 5$ are illustrated in figure 6.16 with the ratios given in figure 6.17. The simulation overestimates the number of particles in the classes 1 to 6, except for small regions at both ends of the interval. With decreasing centrality, the quality of the predictions increases in the region $\eta > -2$. In class seven, EPOS4 starts to underestimate the number of particles within parts of the entire pseudorapidity range. In the classes 8 and 9, the particle count is underestimated over the full range.

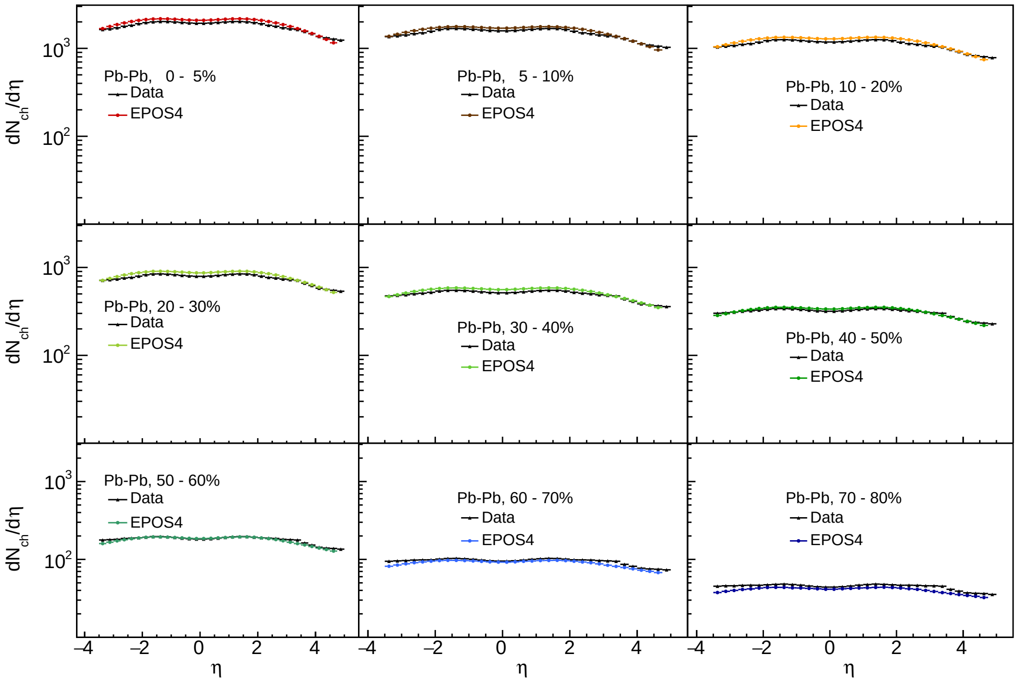

Figure 6.16: Pseudorapidity distributions of Pb-Pb collisions at $\sqrt{s_{\mathrm{NN}}} = 5.02\,\mathrm{TeV}$ for nine centrality classes with in comparison to datasets from the ALICE experiment. Systematic and statistical uncertainties of the data are added in quadrature in this case.

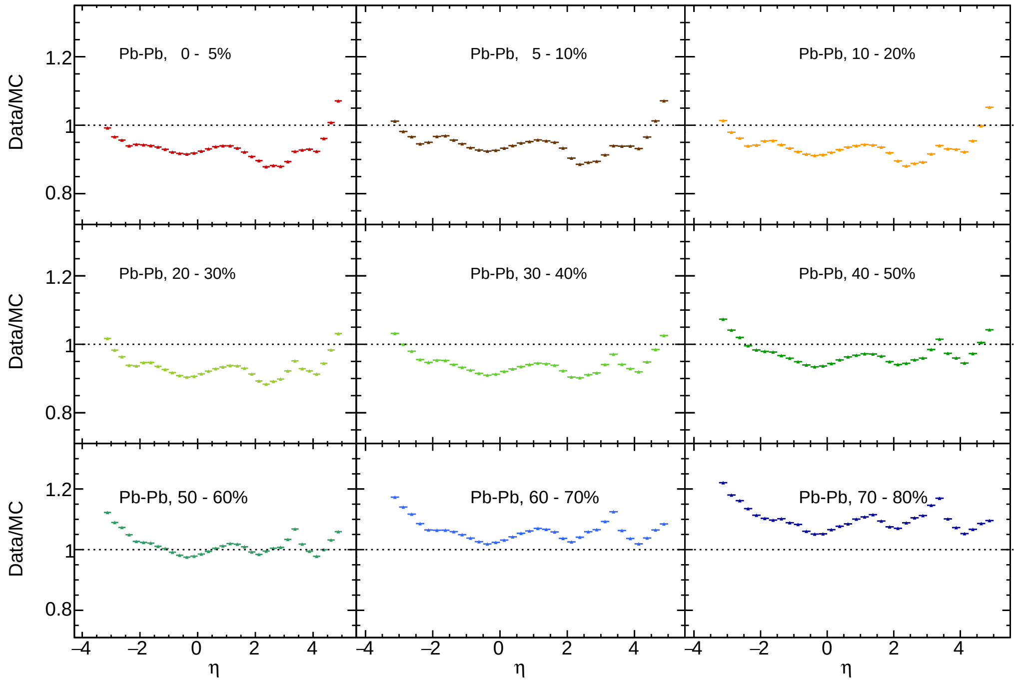

Figure 6.17: Ratios of pseudorapidity distributions for Pb-Pb from figure 6.16.

7 Conclusion and Outlook

In this thesis, pp, p-Pb, and Pb-Pb collisions were simulated using EPOS4. The transverse-momentum distribution, pseudorapidity distribution, charged-particle multiplicity, and multiplicity dependence of the mean transverse momentum were calculated for each collision type. Furthermore, the Pb-Pb collisions were sorted into nine centrality classes, and the transverse-momentum distribution, nuclear modification factor, and pseudorapidity distribution were calculated for each class. All distributions were then compared with datasets provided by the ALICE experiment at CERN.

In pp collisions, the transverse-momentum distribution and the $\langle p_{\mathrm{T}} \rangle$-multiplicity dependence agree well with the ALICE data. The charged-particle multiplicity and pseudorapdidity distributions exhibit greater deviations from the data. The multiplicity is first underestimated below $N_{\mathrm{ch}} < 6$ and reaches a plateau in between 6 to 10, for $N_{\mathrm{ch}} > 10$, the simulation and the data diverge from each other, where the ALICE data have a greater slope than the simulation. The pseudorapidity distribution varies between 54 to 60 percentage points; however, it shows behavior similar to that of the ALICE dataset.

For central p-Pb collisions, EPOS4 differs in the low-p_{T} region $< 1\,\mathrm{GeV}$ of the transverse-momentum distributions by 60 to 30 percentage points. In the range of $1\,\mathrm{GeV}$ to $10\,\mathrm{GeV}$, the distributions still differ by up to 30 percentage points. The pseudorapidity is overestimated by up to 75 percentage points in the $-5 < \eta < 0$ region, but has the same shape as the ALICE dataset. In the $\eta > 0$ regime, the shape of the simulation changes, leading to the intersection of the EPOS4 and ALICE curves. Moreover, EPOS4 is unable to reproduce the shape of the charged-particle multiplicity in p-Pb. Below $N_{\mathrm{ch}} \approx 40$, the multiplicity builds two peaks and valleys, which are features not appearing in the ALICE data. Above this value, the simulation and data distributions diverge. In addition, the $\langle p_{\mathrm{T}} \rangle$-multiplicity dependence is not well predicted. For $N_{\mathrm{ch}} > 20$, the difference is at 40 percentage points with an increase to 50 percentage points at $N_{\mathrm{ch}} \approx 110$. EPOS4 overestimates the total amount of charged particles produced within a p-Pb collision, which can be seen in the charged-particle multiplicity as well as in the transverse-momentum distribution.

In Pb-Pb collisions, the agreement in the transverse-momentum distributions is within 30 percentage points in the low-p_{T} region $< 1\,\mathrm{GeV}$. The simulation does not reproduce the turning point in the spectra at approximately 4 GeV well. After 8 GeV, the distributions differ by less than 30 percentage points again, but with increasing statistical uncertainties. This holds for minimum-bias and centrality-sorted collisions. The charged-particle multiplicity is predicted well in the minimum-bias case with a deviation of less than 30 percentage points, except at a high N_{ch}, where EPOS4 does not predict a steeper decrease in the multiplicity at $N_{\mathrm{ch}} \approx 3050$, but rather decreases further and shows a drop in multiplicity around $N_{\mathrm{ch}} \approx 4150$. The multiplicity dependence of $\langle p_{\mathrm{T}} \rangle$ differs by less than 19 percentage points above $N_{\mathrm{ch}} \approx 1000$. Below this value, the ratio begins to rise from unity to the constant plateau mentioned above.

In the centrality sorted case, the nuclear modification factors agree well in the low- p_{T} region < 1 GeV well in each class, but are unable to rise to the same height as the data. This is consistent with the deviation in the transverse-momentum distributions of pp and Pb-Pb. The pseudorapidity distributions are well predicted in each class with a deviation of less than 10 percentage points in the mid-rapidity interval $\eta < |2|$. In the boundary regions of the interval, the deviation increases up to 20 percentage points.

In general, EPOS4 can simulate the ALICE data in a high-p_{T} region above 10 GeV with a good accuracy in all cases but fails to predict the charged-particle multiplicities in the pp and p-Pb cases as well as the pseudorapidity distribution in the p-Pb case. The high deviations in p-Pb collisions are probably mainly explained by the missing parameterized fluid expansion. In Pb-Pb collisions, all observables are predicted with higher accuracy than in pp and p-Pb collisions. The higher deviations in the pp and p-Pb cases may be explained by the overestimation of QGP effects in these collisions.

In further investigations, it might be of interest to study more aspects of heavy-ion collisions with EPOS4, such as charmonium or identified charged-particle production. Comparisons not only to measured data but also to other MC event generators may be useful. Additionally, options for parallel executions of a larger number of events as well as the possibility to store only user-selected information per event in the output file would increase the usability of the EPOS4 event generator by far. The implementation of such features in EPOS4 could also lead to interesting projects.

A Appendix

Template options file for EPOS4

```
application hadron
set laproj $ATOMIC_NUM_PROJECTILE
set maproj $MASS_NUM_PROJECTILE
set latarg $ATOMIC_NUM_TARGET
set matarg $MASS_NUM_TARGET

set ecms $ECMS
set istmax 25
set iranphi 1
ftime on
nodecays 120 -120 130 -130 1120 end

set ninicon $NINICON
core $CORE
hydro $HYDRO
eos $EOS
hacas $HACAS
set nfull $NFULL
set nfreeze $NFREEZE
set modsho $MODSHO
set centrality $CENTRALITY

fillTree4(C1)
```

The listing describes the EPOS4 options file template used throughout this thesis. All values that start with the dollar sign $ must be replaced with the values for the corresponding collision type.

Pseudorapidity distributions in p-Pb collisions

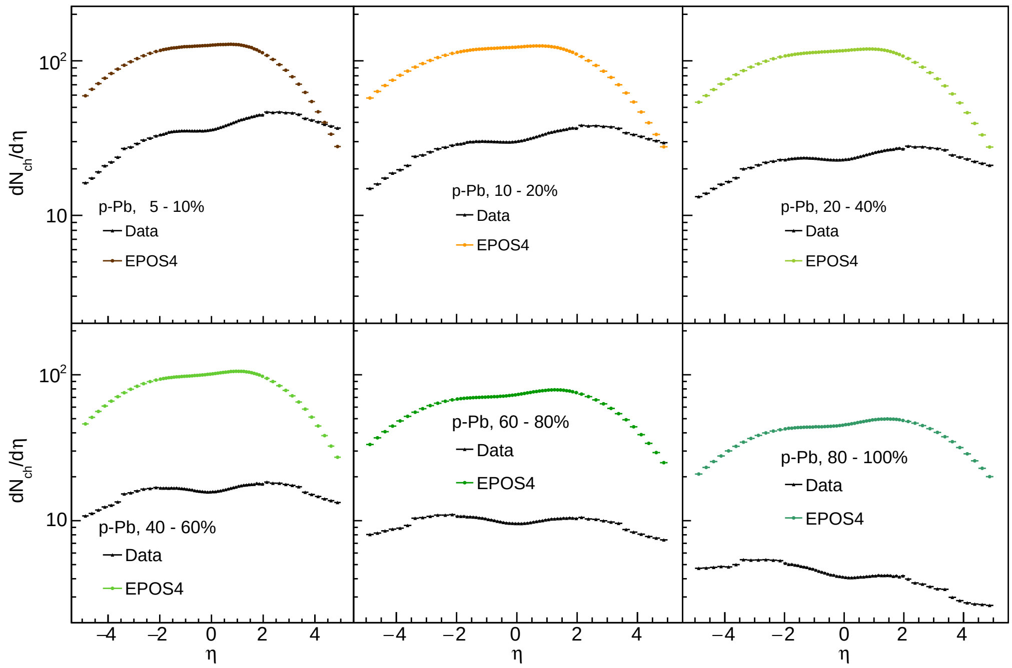

Figure A.1: Pseudorapidity distributions of p-Pb collisions at $\sqrt{s_{\mathrm{NN}}} = 5.02\,\mathrm{TeV}$ for six centrality classes with in comparison to datasets from the ALICE experiment. Systematic and statistical uncertainties of the data are added in quadrature in this case.

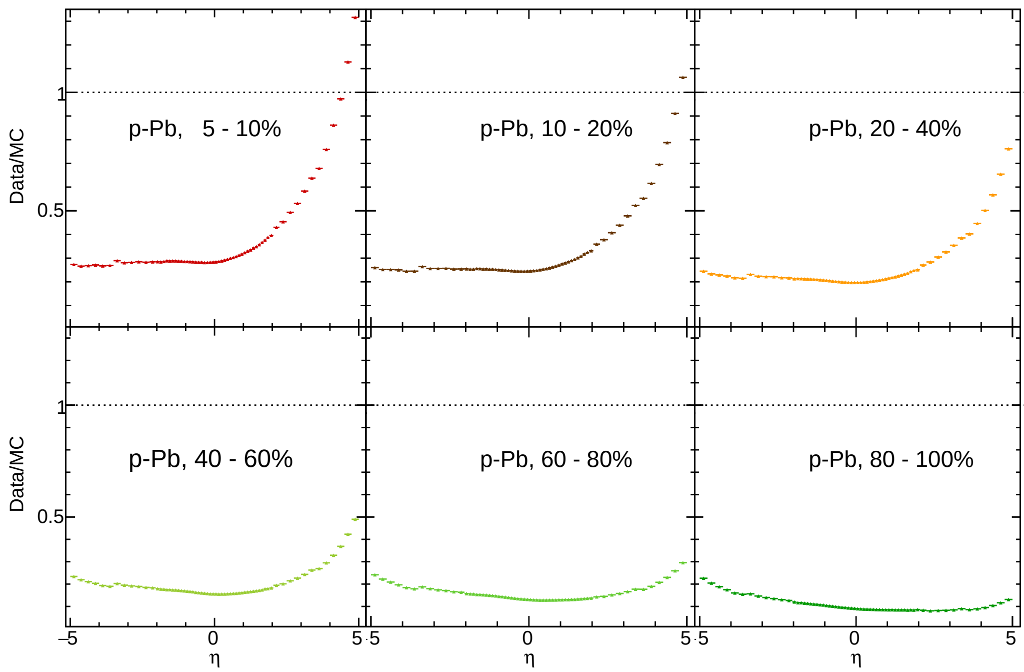

Figure A.2: Ratios of pseudorapidity distributions for p-Pb from figure A.1.

Table A.1: Impact parameter range together with the corresponding centrality interval each centrality class determined with EPOS4 in comparison to data for p-Pb collisions.

Class	Centrality	b [fm]
1	0 % to 5 %	0.0 to 1.71
2	5 % to 10 %	1.71 to 2.42
3	10 % to 20 %	2.42 to 3.42
4	20 % to 40 %	3.42 to 4.87
5	40 % to 60 %	4.87 to 6.04
6	60 % to 80 %	6.04 to 7.20
7	80 % to 100 %	7.20 to 9.0

Transverse Momentum Spectra of charged particles in Pb-Pb

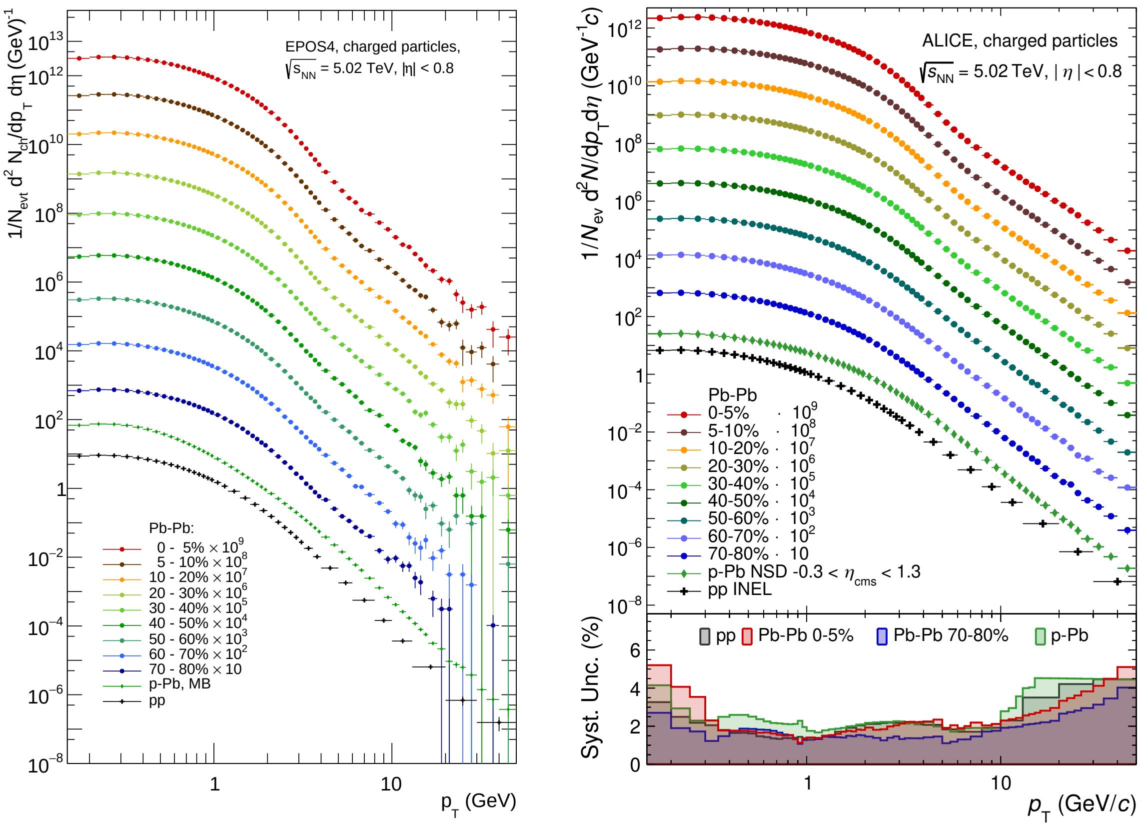

Figure A.3: The figures show the transverse-momentum distributions of Pb-Pb collisions in nine classes of centrality at $\sqrt{s_{\mathrm{NN}}} = 5.02\,\mathrm{TeV}$ in a pseudorapidity interval of $\eta < |0.8|$ calculated in EPOS4 (left) and measured by the ALICE experiment (right) [Gro18].

For each centrality class, the transverse momentum distribution is shown in figure A.3 on the left alongside the ALICE measurements on the right side. The classes are scaled by powers of ten, such that the most central class appears on the top of the histogram, for better visibility. Additionally, the transverse momentum distributions of p-Pb and pp collisions are presented in the same histogram. Like in the discussion of the transverse momentum distributions in section 6.4, one observes a turning point around $p_{\mathrm{T}} \approx 6\,\mathrm{GeV}$. With decreasing centrality, the shape of the Pb-Pb distributions approaches the shape of the pp distributions.

Bibliography

[ABM04] A. Andronic and P. Braun-Munzinger. Ultrarelativistic nucleus–nucleus collisions and the quark–gluon plasma. *Lecture Notes in Physics*, page 35–67, Dec 2004. 5

[AGK+20] Eemeli Annala, Tyler Gorda, Aleksi Kurkela, Joonas Nättilä, and Aleksi Vuorinen. Evidence for quark-matter cores in massive neutron stars. *Nature Physics*, 16(9):907–910, Sep 2020. 5

[CER] CERN. Root. `https://root.cern/`. [Online; last accessed 08-August-2023]. 17

[Col04] The ALICE Collaboration. *ALICE forward detectors: FMD, TO and VO: Technical Design Report*. Technical design report. ALICE. CERN, Geneva, 2004. Submitted on 10 Sep 2004. 12

[Col07] The ALICE Collaboration. THE ALICE FORWARD MULTIPLICITY DETECTOR. *International Journal of Modern Physics E*, 16(07n08):2432–2437, aug 2007. 12

[Col08] The ALICE Collaboration. The alice experiment at the cern lhc. *Journal of Instrumentation*, 3(08):S08002, aug 2008. 10

[Col10] The ALICE Collaboration. The ALICE TPC, a large 3-dimensional tracking device with fast readout for ultra-high multiplicity events. *Nuclear Instruments and Methods in Physics Research Section A: Accelerators, Spectrometers, Detectors and Associated Equipment*, 622(1):316–367, oct 2010. 12

[Col13a] The ALICE Collaboration. Centrality determination of pb-pb collisions at $\sqrt{s_{NN}}$ = 2.76 tev with alice. *Physical Review C*, 88(4), oct 2013. 27

[Col13b] The ALICE Collaboration. Upgrade of the ALICE Time Projection Chamber. Technical report, CERN, 2013. 11

[Col14] The ALICE Collaboration. Technical Design Report for the Upgrade of the ALICE Inner Tracking System. Technical report, CERN, 2014. 11

[Col18] The ALICE Collaboration. Transverse momentum spectra and nuclear modification factors of charged particles in pp, p-pb and pb-pb collisions at the LHC. *Journal of High Energy Physics*, 2018(11), nov 2018. 8, 12

[Col22] ALICE Collaboration. Multiplicity dependence of charged-particle production in pp, p-pb, xe-xe and pb-pb collisions at the lhc, 2022. 8, 12

[Col23] The ALICE Collaboration. System-size dependence of the charged-particle pseudorapidity density at $\sqrt{s_{\mathrm{NN}}} = 5.02$ TeV for pp, p pb, and pb-pb collisions. *Physics Letters B*, page 137730, feb 2023. 12

[EG21] Communications Education and Outreach Group. Lhc - the guide. Technical report, CERN, 2021. [Online; last accessed 06-August-2023]. 9, 10

[GKL+99] M Gallio, W Klempt, L Leistam, J De Groot, and Jürgen Schükraft. *ALICE Zero-Degree Calorimeter (ZDC): Technical Design Report.* Technical design report. ALICE. CERN, Geneva, 1999. 12

[Gro18] Julius Maximilian Gronefeld. *Transverse Momentum Distributions and Nuclear Modification Factors in Heavy-Ion Collisions with ALICE at the Large Hadron Collider.* PhD thesis, Technische Universität, Darmstadt, 2018. 5, 7, 11, 12, 37

[Ian14] Edmond Iancu. QCD in heavy ion collisions, 2014. Based on lectures presented at the 2011 European School of High-Energy Physics, 7-20 September 2011, Cheile Gradistei, Romania. 73 pages, many figures. 4

[JS11] Klaus Reygers Johanna Stachel. Qgp physics - from fixed target to lhc 2. kinematic variables. `https://www.physi.uni-heidelberg.de/~reygers/lectures/2011/qgp/qgp_02_kinematics.pdf`, 2011. [Online; last accessed 27-August-2023]. 5

[McI16] Brett McInnes. A rotation/magnetism analogy for the quark plasma. *Nuclear Physics B*, 911, 04 2016. 4

[Mis23] Cush MissMJ. Standard Model — Wikipedia, the free encyclopedia. `https://en.wikipedia.org/wiki/Standard_Model`, 2023. This file is licensed under the Creative Commons Attribution 3.0 Unported license. [Online; last accessed 28-June-2023]. 2

[Mob16] Esma Mobs. The CERN accelerator complex. Complexe des accélérateurs du CERN, 2016. General Photo. 9

[MRSS07] Michael L. Miller, Klaus Reygers, Stephen J. Sanders, and Peter Steinberg. Glauber modeling in high-energy nuclear collisions. *Annual Review of Nuclear and Particle Science*, 57(1):205–243, nov 2007. 6

[PPR83] G. Parisi, R. Petronzio, and F. Rapuano. A measurement of the string tension near the continuum limit. *Physics Letters B*, 128(6):418–420, 1983. 3

[Sch13] Matthew D. Schwartz. *Quantum Field Theory and the Standard Model*. Cambridge University Press, 2013. 14

[Str14] M. Strickland. Anisotropic hydrodynamics: Three lectures. *Acta Physica Polonica B*, 45(12):2355, 2014. 5

[Tau17] Arturo Tauro. ALICE Schematics, 2017. General Photo. 10

[Tho09] Mark Thomson. Particle Physics - handout 8: Quantum chromodynamics. `https://www.hep.phy.cam.ac.uk/~thomson/lectures/partIIIparticles/Handout8_2009.pdf`, 2009. [Online; last accessed 28-June-2023]. 3

[Tho13] Mark Thomson. *Modern particle physics*. Cambridge University Press, New York, 2013. 2, 14

[Wer07] Klaus Werner. Core-corona separation in ultra-relativistic heavy ion collisions. *Phys. Rev. Lett.*, 98:152301, 2007. 15

[Wer22] Klaus Werner. Epos4. `https://klaus.pages.in2p3.fr/epos4`, 2022. [Online; last accessed 08-August-2023]. 13

[Wer23a] K. Werner. Core-corona procedure and microcanonical hadronization to understand strangeness enhancement in proton-proton and heavy ion collisions in the epos4 framework, 2023. 13, 15

[Wer23b] Klaus Werner. On a deep connection between factorization and saturation: new insight into modeling high-energy proton-proton and nucleus-nucleus scattering in the epos4 framework, 2023. 13, 14

[WGKP14] K. Werner, B. Guiot, Iu. Karpenko, and T. Pierog. Analyzing radial flow features in p-pb and p-p collisions at several tev by studying identified-particle production with the event generator epos3. *Phys. Rev. C*, 89:064903, Jun 2014. 15

Declaration of Academic Integrity

I, *Alexander Tiekötter*, hereby confirm that this thesis, entitled "Monte Carlo simulation of charged-particle production in Heavy-Ion Collisions with EPOS4" is solely my own work and that I have used no sources or aids other than the ones stated. All passages in my thesis for which other sources, including electronic media, have been used, be it direct quotes or content references, have been acknowledged as such and the sources cited. I am aware that plagiarism is considered an act of deception which can result in sanction in accordance with the examination regulations.

Münster, September 15, 2023

Alexander Tiekötter

I consent to having my thesis cross-checked with other texts to identify possible similarities and to having it stored in a database for this purpose.

I confirm that I have not submitted the following thesis in part or whole as an examination paper before.